HIGH PRECISION STUDY OF MUON CATALYZED FUSION IN D₂ AND HD GASES

D. V. Balin [a], V. A. Ganzha [a], S. M. Kozlov [a], E. M. Maev [a],
G. E. Petrov [a], M. A. Soroka [a], G. N. Schapkin [a], G. G. Semenchuk [a],
V. A. Trofimov [a], A. A. Vasiliev [a], A. A. Vorobyov [a], N. I. Voropaev [a],
C. Petitjean [b], B. Gartner [c], B. Lauss [c,1], J. Marton [c,2],
J. Zmeskal [c,2], T. Case [d], K. M. Crowe [d], P. Kammel [d,3],
F. J. Hartmann [e], M. P. Faifman [f]

[a] Petersburg Nuclear Physics Institute (PNPI), Gatchina, Russia
[b] Paul Scherrer Institute (PSI), Villigen, Switzerland
[c] Institute for Medium Energy Physics, Austrian Academy of Sciences, Wien
[d] University of California Berkeley (UCB) and LBNL, Berkeley, USA
[e] Technical University of Munich (TUM), Garching, Germany
[f] National Research Centre «Kurchatov Institute», Moscow

*Present address: Paul Scherrer Institute (PSI), CH-5232 Villigen, Switzerland.
**Present address: Stefan-Meyer-Institute for Subatomic Physics (SMI), A-1090 Wien, Austria.
***Present address: University of Illinois at Urbana-Champaign, Urbana, IL 61801, USA.

HIGH PRECISION STUDY OF MUON CATALYZED FUSION IN D_2 AND HD GASES

D. V. Balin [a], V. A. Ganzha [a], S. M. Kozlov [a], E. M. Maev [a],
G. E. Petrov [a], M. A. Soroka [a], G. N. Schapkin [a], G. G. Semenchuk [a],
V. A. Trofimov [a], A. A. Vasiliev [a], A. A. Vorobyov [a], N. I. Voropaev [a],
C. Petitjean [b], B. Gartner [c], B. Lauss [c,1], J. Marton [c,2],
J. Zmeskal [c,2], T. Case [d], K. M. Crowe [d], P. Kammel [d,3],
F. J. Hartmann [e], M. P. Faifman [f]

[a] Petersburg Nuclear Physics Institute (PNPI), Gatchina, Russia
[b] Paul Scherrer Institute (PSI), Villigen, Switzerland
[c] Institute for Medium Energy Physics, Austrian Academy of Sciences, Wien
[d] University of California Berkeley (UCB) and LBNL, Berkeley, USA
[e] Technical University of Munich (TUM), Garching, Germany
[f] National Research Centre «Kurchatov Institute», Moscow

Muon catalyzed dd fusion in D_2 and HD gases in the temperature range from 28 to 350 K was investigated in a series of experiments based on a time-projection ionization chamber operating with pure hydrogen. The final analysis of the data together with a comprehensive comparison with calculations based on recent μCF theory are presented in this work. All main characteristics of the chain of accompanying reactions including the resonant and nonresonant $dd\mu$ formation rates, the rate for hyperfine transitions in $d\mu$ atoms, the branching ratio of the two charge symmetric fusion channels $^3\text{He} + n$ and $t + p$ and the muon sticking probability were extracted from data measured with high absolute precision. The obtained energy $\varepsilon_{11}(\text{fit}) = -1.9651(7)$ eV of the loosely bound $dd\mu$ molecule state responsible for the high rate of resonant molecule formation is in impressive agreement with the latest theoretical results $\varepsilon_{11}(\text{theory}) = -1.9646$ eV.

Проведены исследования мюонного катализа dd-синтеза в газах D_2 и HD в диапазоне температур от 28 до 350 K с использованием ионизационной камеры, наполненной чистым водородом. В данной работе представлены результаты завершенного анализа данных и проведено детальное сравнение с последними теоретическими расчетами по мюонному катализу. С высокой абсолютной точностью определены из экспериментальных данных все основные характеристики цепочки сопровождающих процессов, в том числе резонансная и нерезонансная скорости образования молекул $dd\mu$, скорости переворота спина мюона при столкновении $d\mu$-атома, отношение выходов двух зарядово-симметричных каналов синтеза $^3\text{He} + n$ и $t + p$, а также коэффициент прилипания мюона. Энергия $\varepsilon_{11}(\text{fit}) = -1{,}9651(7)$ эВ слабосвязанного состояния $dd\mu$, ответственного за высокую величину скорости резонансного образования молекул, находится в хорошем согласии с последним теоретическим результатом $\varepsilon_{11}(\text{theory}) = -1{,}9646$ эВ.

PACS: 36.10.Ee; 25.30.Mr; 29.40.Cs

---

[1]Present address: Paul Scherrer Institute (PSI), CH-5232 Villigen, Switzerland.
[2]Present address: Stefan-Meyer-Institute for Subatomic Physics (SMI), A-1090 Wien, Austria.
[3]Present address: University of Illinois at Urbana-Champaign, Urbana, IL 61801, USA.

INTRODUCTION

In this Section, we consider the milestones of the history of muon catalyzed fusion (μCF) related mainly to dd fusion. The description of other aspects of μCF studies can be found in several review articles [1].

The idea of the μCF process was first suggested by Frank [2] in 1947 when he tried to find an alternative explanation of the observations by Powell and his group [3]. This experiment had detected some cosmic particles stopped in the photoemulsion with the emission of $\sim$5 MeV muons from the end of the primary track. By that time, muons were the only particles identified in cosmic rays. The observation established the existence of a new particle, called later the π meson, decaying into the muon and neutrino. Frank pointed out that the negatively charged muons may have some probability to be captured by deuterons present in the photoemulsion thus forming small neutral objects, $d\mu$ atoms. Like neutrons, the $d\mu$ atoms can travel in matter and easily penetrate inside molecules. If the $d\mu$ atom comes close enough to a proton, this might lead to a fusion reaction $d\mu + p \rightarrow {}^3\mathrm{He} + \mu + 5.5$ MeV with the track picture similar to those observed. In the above explanation, the muon plays the role of a catalyzer of the fusion reaction. Though this interpretation of Powell's experiment was excluded (the probability to form the $d\mu$ atoms in photoemulsions is negligible), the concept of muon catalyzed fusion had been born.

A specific mechanism for the fusion reaction was first suggested by Sakharov [4] in 1948 with the key point being the formation of muonic molecules, such as the $dd\mu$ molecule. This molecule is an analog of the singly ionized ordinary deuterium molecule D_2^+. However, due to the larger mass of the muon, the size of the $dd\mu$ molecule is about 200 times less than that of the D_2^+ ion. Therefore, the two deuterons in the $dd\mu$ molecule are enclosed in a small volume within a distance of ~ 500 fm between them with a strongly reduced width of the repulsive Coulomb barrier. As a result, the probability for quantum penetration through the barrier proves to be so high that the fusion reaction takes place with a rate much higher than the muon decay rate $\lambda_0 = 0.45516 \cdot 10^6$ s^{-1}. The striking feature of this mechanism is that, unlike the thermonuclear fusion which requires very high temperatures ($\sim 50 \cdot 10^6$ K), the muon catalyzed fusion occurs at normal temperatures.

The next important step was to understand the mechanism of muonic molecule formation. In the model formulated by Zeldovich [5] in 1954, the formation of the $dd\mu$ molecule occurs inside the D_2 molecule with the energy gained upon binding the $dd\mu$ molecule being carried off by an ejected electron:

$$d\mu + \mathrm{D}_2 \rightarrow [(dd\mu)de]^+ + e^-. \tag{1}$$
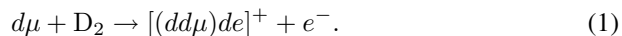
Experimentally, the first μCF reaction was discovered by Alvarez and his coworkers [6] in 1956. As a by-product of their experiment with the Berkeley

hydrogen bubble chamber, they observed the pd fusion reaction catalyzed by negative muons stopped in the bubble chamber, just the fusion channel first considered by Frank. This accidental discovery triggered intensive experimental and theoretical studies of the μCF physics. In particular, the $dd\mu$ fusion reaction $d\mu + d \rightarrow t + p + \mu + 4.03$ MeV was observed [6], and its rate was studied in the experiments with liquid deuterium bubble chambers [7, 8]. The measured μCF rates appeared to be quite low, the $dd\mu$ molecule formation rate, $\lambda_{dd\mu} \approx 0.1 \cdot 10^6$ s^{-1}, being smaller than the muon decay rate. These results were in fairly good agreement with the Zeldovich model [9].

Some surprise, however, came from an experiment [10] performed at Dubna in 1966. In this experiment, the $pd\mu$ and $dd\mu$ fusion was studied using a hydrogen/deuterium filled diffusion chamber operating at 250 K. The puzzling result was the unexpectedly large $dd\mu$ molecule formation rate, by an order of magnitude exceeding the value of $\lambda_{dd\mu}$ observed at liquid hydrogen temperature. Neither the large value of $\lambda_{dd\mu}$ nor its strong temperature dependence could be explained on the basis of the Auger process, Eq. (1). To resolve this problem, Vesman suggested in 1967 [11] that the $dd\mu$ molecule may have a very loosely bound state, so that the released energy is small enough to be completely absorbed in vibrations and rotations of the resulting compound molecule:

$$d\mu + D_2 \rightarrow [(dd\mu)dee]^*. \tag{2}$$
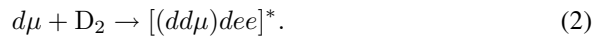
This is a resonant process increasing considerably the $dd\mu$ molecule formation rate. Also, its temperature dependence is explained as tuning of the kinetic energy of the $d\mu$ atom to resonance condition.
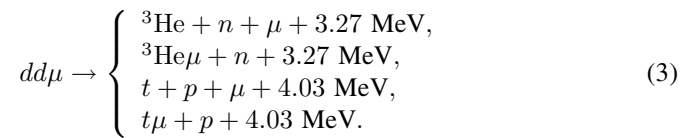
The calculation of these $dd\mu$ molecule energy levels turned out to be a difficult task. Only a decade later Ponomarev and his collaborators developed a high precision method for the description of the three-body Coulomb system [12] which established that such a loosely bound state does indeed exist in the $dd\mu$ and $dt\mu$ molecules with the binding energies ≈ 2 and ≈ 1 eV, respectively, well below the dissociation energy of the D_2 molecule (4.5 eV). In 1977, applying the resonant molecular formation mechanism, the temperature dependence of the $dd\mu$ formation rate was calculated and a very high $dt\mu$ molecule formation rate was predicted [13] which might exceed the muon decay rate by orders of magnitude. Soon, in 1979, this prediction was confirmed by a Dubna experiment [14] reporting $\lambda_{dt\mu} \approx 10^8$ s^{-1}.

The possibility that, based on resonant $dt\mu$ formation, a single muon could catalyze ≈ 100 fusions and release a substantial amount of energy was discussed by Gershtein and Ponomarev [15] and triggered a burst of interest in the field. New experimental programmes were started in all laboratories with muon beams, while the theoretical efforts were even more widespread. Partly, these efforts were motivated by the revived hopes to use the $dt\mu$ fusion for practical applications.

On the other hand, the μCF process is of great interest by itself, allowing to study various aspects of mesoatomic, mesomolecular and nuclear physics. From this point of view, the $dd\mu$ fusion proved to have important advantages. In contrast to the more complicated processes in $dt\mu$ fusion, $dd\mu$ fusion allows unambiguous quantitative theoretical description. Therefore, comparison of experimental data on dd fusion with theoretical calculations is of primary importance for understanding the μCF phenomena.

An important step in this programme was the observation by the Vienna–PSI collaboration that the $dd\mu$ molecule formation rate strongly depends on the total spin of the $d\mu$ atom, $F = 3/2$ or $F = 1/2$ — another convincing evidence of the resonant formation of the muonic molecules. It was shown that measurements of the temperature dependence of the $dd\mu$ formation rates $\lambda_{dd\mu}^{3/2}(T)$ and $\lambda_{dd\mu}^{1/2}(T)$ provide a sensitive test of the various elements of the resonant $dd\mu$ formation mechanism. These experiments were performed in a high intensity muon beam at PSI during 1979–1990 [16, 17]. The muons were stopped in a D_2 liquid or gas target, and the time distribution of the neutrons produced in the dd fusion reaction was measured by a set of neutron detectors surrounding the target.

The $dd\mu$ fusion leads to four reaction channels[1]:

$$dd\mu \rightarrow \begin{cases} {}^3\text{He} + n + \mu + 3.27 \text{ MeV}, \\ {}^3\text{He}\mu + n + 3.27 \text{ MeV}, \\ t + p + \mu + 4.03 \text{ MeV}, \\ t\mu + p + 4.03 \text{ MeV}. \end{cases} \qquad (3)$$

A new experimental method developed at PNPI (Gatchina) allowed one to detect simultaneously all the $dd\mu$ fusion channels. In this method, a deuterium-filled high pressure ionization chamber was used as a sensitive target detecting both the stopped muons and the charged fusion products: ^{3}He, ^{3}Heμ, and $t + p$. A series of $dd\mu$ fusion experiments was carried out by the PNPI group in 1982–1988 [18] using the muon channel of the Gatchina synchrocyclotron. These experiments allowed one to measure for the first time the ^{3}Heμ sticking probability and the yield ratio of the charge symmetric fusion channels $R = Y({}^3\text{He} + n)/Y(t + p)$. Surprisingly, it was found that this ratio is quite different for dd fusion following resonant and nonresonant formation of the $dd\mu$ molecule.

The Gatchina experiments demonstrated that the new active target method provided high absolute precision in measurements of the main parameters of the $dd\mu$ fusion process, but statistics were limited by the low beam intensity at PNPI. In 1989, a new μCF collaboration started experiments at the high intensity μE4 muon beam at the Paul Scherrer Institute with an ionization chamber as its central

---

[1]In the present work we do not consider the fifth channel, the reaction of the dd radiative capture $dd\mu \rightarrow {}^4\text{He}\mu + \gamma + 23.8$ MeV, which takes place with a very low branching.

element. The first experiments in 1989–1993 were the direct observation of the muon sticking probability in $dt\mu$ fusion [19] and the high precision measurements of the μ^3He nuclear capture rate [20]. After that, the μCF collaboration returned to renewed studies of the $dd\mu$ fusion with the goal to investigate with high precision both the resonant and nonresonant μCF processes in D_2 and HD gases in a wide temperature range from 28 to 350 K. These experiments were performed in 1994–1996. Preliminary results were presented in several conference reports [21]. This paper presents the final report on the experimental technique, the data analysis and all experimental results obtained in this experimental programme, and provides a comprehensive comparison with the presently available theories of muon catalyzed fusion.

1. μCF KINETICS IN GAS MIXTURES OF DEUTERIUM WITH HYDROGEN

Figure 1 shows the kinetics scheme of the μCF processes in D_2, $D_2 + H_2$, and HD gases. Initially, the muon entering the hydrogen gas target is slowed down to an energy of ~ 10 eV, where it is captured by a hydrogen molecule forming a $p\mu$ or $d\mu$ atom in an excited state. The de-excitation of the muonic atoms

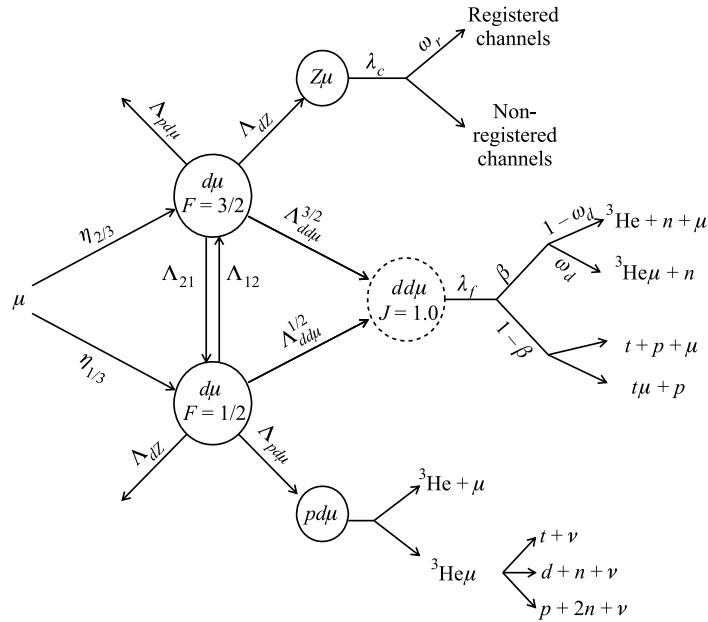Fig. 1. Scheme of the μCF kinetics in D_2/HD/H_2 gas mixtures. Muon decay with the rate λ_0 occurs from all states

proceeds mainly by ejection of electrons from the target molecules (external Auger effect), by radiative transitions, and by Coulomb collisions. These processes are quite fast in a dense hydrogen target and the $1s$-ground state will be reached in less than ≈ 1 ns at our experimental conditions. The theory predicts some increase of the kinetic energy of the muonic atoms during the cascade process due to collisions [22, 23] supported by experimental evidence [24–26]. In our experimental conditions, the initial kinetic energy of the $p\mu(1s)$ and $d\mu(1s)$ atoms will be peaked around 1–2 eV with possible tails up to 200 eV. In case the muon has formed a $p\mu$ atom, it can be transferred to a $d\mu$ atom from either the excited or the ground state of the $p\mu$ atom [27–29]. In this case the $d\mu$ atoms receive kinetic energy up to 43 eV according to the reaction:

$$p\mu(n) + d \rightarrow d\mu(n) + p + \frac{135}{n^2} \text{ eV.} \tag{4}$$
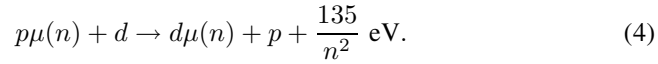
The rate of this reaction at our experimental conditions is $(3.5-7) \cdot 10^8$ s^{-1} [30] depending on the deuterium concentration in the gas mixture. This means that all muons stopped in the target should be transferred to the $d\mu$ atoms in less than 10 ns. Then the $d\mu$ atoms start to lose their kinetic energy in elastic scattering on deuterons (protons) and, at the energies below 1 eV, on the hydrogen molecules. At our experimental conditions, full thermalization of the $d\mu$ atoms is expected to be reached after ~ 100 ns in the D$_2$ gas and after ~ 200 ns in the HD gas [31]. Note that the time distributions measured in our experiment are those of the first fusion in the μCF cycle as observed in the ionization chamber. In this case, the generation of epithermal muonic atoms following muon recycling after fusion is not relevant and our observed rates converge to their thermalized limit after initial thermalization. This conclusion was confirmed by Adamczak with Monte Carlo calculations analogous to those in [32].

After the de-excitation cascade, the two $d\mu$ spin states $F = 3/2$ and $F = 1/2$ are expected to be populated according to their statistical weights ($\eta_{3/2} = 2/3$ and $\eta_{1/2} = 1/3$). So, the initial state of the $d\mu$ atoms appears to be well defined, and this is of primary importance for quantitative consideration of the subsequent μCF processes.

1.1. Formation of the $dd\mu$ Molecule and Back-Decay. There are five bound energy states for the $dd\mu$ molecule defined by the rotational (J) and vibratio- nal (v) quantum numbers (Table 1). The loosely bound state ($J = 1$, $v = 1$) can be formed by resonant formation, the other states can be populated either by de-excitation of the (1,1) state or by direct $dd\mu$ formation via the nonresonant mechanism. The $dd\mu$ molecule can be formed in collisions of $d\mu$ atoms in the $F = 3/2$ or $F = 1/2$ hyperfine states with deuterons bound in D$_2$ and HD. In case of resonant $dd\mu$ formation, this process is accompanied by back-decay of the muonic molecular complex [35–37]:

$$(d\mu)_F + D_2 \rightarrow [(dd\mu)dee]^* \rightarrow (d\mu)_{F'} + D_2. \tag{5}$$
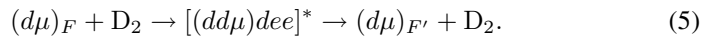
Owing to the exchange symmetry of the $dd\mu$ molecule, the de-excitation rate of the complex $[(dd\mu)dee]^*$ is comparatively slow. Therefore, the back-decay can occur before the dd fusion reaction takes place. The experimentally determined rates $\Lambda_{dd\mu}^{3/2}$ and $\Lambda_{dd\mu}^{1/2}$ entering the kinetics scheme shown in Fig. 1 are the *effective* $dd\mu$ formation rates, i.e., the rates of those $dd\mu$ formation processes which actually lead to fusion.

Table 1. **Nonrelativistic $dd\mu$ binding energies $|\epsilon_{Jv}|$ compiled from the data of [33, 34]**

(J, v)	Binding energy, eV
(0,0)	325.074
(0,1)	35.844
(1,0)	226.682
(1,1)	1.974985
(2,0)	86.494

1.2. Hyperfine Transitions in $d\mu$ Atoms. The energy difference between the $d\mu$ hyperfine states $F = 3/2$ and $F = 1/2$ is $\Delta = 0.0485$ eV [38]. The rates $\Lambda_{21}^{\mathrm{sc}}$ and $\Lambda_{12}^{\mathrm{sc}}$ for the hyperfine transitions $(3/2 \to 1/2)$ and $(1/2 \to 3/2)$, respectively, occuring in collisions of the $d\mu$ atom with D$_2$(HD) molecules, were first calculated by Gershtein [39]. In case of resonant formation of the $dd\mu$ molecule, there is also a contribution due to the back-decay (Eq. (5)) with rates $\Lambda_{FF'}^{\mathrm{bd}}$. Then, the total hyperfine transition rates are given by the sum $\Lambda_{FF'} = \Lambda_{FF'}^{\mathrm{sc}} + \Lambda_{FF'}^{\mathrm{bd}}$ and are related by the detailed balance equation

$$\Lambda_{12} = 2\,\mathrm{e}^{-\Delta/kT}\Lambda_{21}, \qquad (6)$$

where $k = 8.62 \cdot 10^{-5}$ eV/K.

1.3. Nuclear dd Fusion. The dd fusion rate λ_f depends on the quantum numbers of the $dd\mu$ state from which fusion occurs. In particular, theory predicts $\lambda_f = 0.44 \cdot 10^9$ s^{-1} for the (1,1) state and $\lambda_f = 1.5 \cdot 10^9$ s^{-1} for the (1,0) state [40]. In the symmetric $dd\mu$ molecule, the $\Delta J = 1$ transitions are forbidden, apart from small relativistic effects. The calculated $\Delta J = 0$ transition rate between the (1,1) and (1,0) states is rather low: $\Gamma_{\mathrm{dex}} = 0.02 \cdot 10^9$ s^{-1} [41]. Therefore, after resonant $dd\mu$ formation, fusion takes place nearly exclusively from the (1,1) state. The dd fusion leads to four decay channels shown in Fig. 1 with the branching ratio of the charge symmetric channels $R = \beta/(1-\beta) = Y(^3\mathrm{He} + n)/Y(t + p)$ depending on the angular momentum (J) of the $dd\mu$ state from which the fusion takes place.

1.4. Muon Sticking to ^{3}He. The fusion process in the $dd\mu$ molecule may lead to formation of a $(^3\mathrm{He}\mu)^*$ atom recoiling from the point of dd fusion with kinetic energy 0.8 MeV, the muon being bound in one of the orbits (n, l). This process is called the «initial» muon sticking (i.e., sticking immediately after $dd\mu$ fusion) with probability denoted as ω_d^0. There is a certain probability (defined by the «reactivation coefficient» $\mathcal{R}$) that the muon could be shaken off (muon stripping) during the slowing down of the $(^3\mathrm{He}\mu)^*$ atom in collisions with nuclei of the traversed matter. The probability ω_d for «final» sticking, after the ^{3}Heμ atom came to rest, is defined as $\omega_d = \omega_d^0(1 - \mathcal{R})$.

1.5. Background Reactions. One of the background reactions is the $pd\mu$ fusion through its decay channel $pd\mu \to {}^3\text{He} + \mu + 5.5$ MeV. This background is negligible for the D_2 runs, but it becomes visible in the HD and $H_2 + D_2$ runs. In this experiment, this channel is detected and separated well from the dd-fusion reaction. In addition, the triton from the muon capture reaction $pd\mu \to {}^3\text{He}\mu \to t + \nu$ is detected as well and serves as a monitor for this reaction.

The main (though quite small) background comes from the charged products of the nuclear muon capture by the gas impurities such as N_2 and H_2O with muon capture rates $\lambda_c \approx (7-10) \cdot 10^4$ s^{-1}.

2. EXPERIMENT

2.1. Experimental Setup. The basic element of the setup shown in Fig. 2 is a high pressure cryogenic hydrogen ionization chamber (IC). It operates as an active target and detects both the incoming muons and the charged products from the dd fusion and from the nuclear muon capture reactions. This detector selects
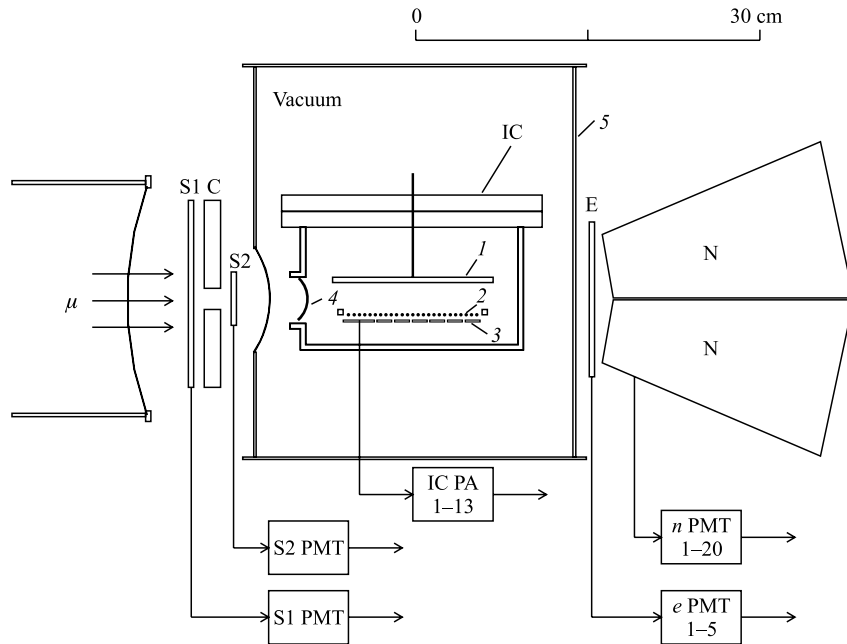

Fig. 2. Scheme of the experimental setup: *1* — cathode; *2* — grid; *3* — anodes of the ionization chamber; *4* — beryllium entrance window; *5* — vacuum vessel; E, N — electron and neutron counters; S1, S2 — beam monitor counters; C — beam collimator; PA — preamplifiers of the readout channels of IC; PMT — photomultiplier tubes

clean muon stops in the IC sensitive volume, well separated in space from the chamber electrodes, and provides close to 100% efficiency in detection of the dd fusion events. The IC was surrounded by an array of plastic counters for detection of 2.45 MeV neutrons from the fusion reaction $dd \rightarrow {}^3\text{He} + n$. This array contained 20 neutron counters with five 2.5 mm thick detectors in front of them to veto muon decay electrons. The total detection efficiency for dd fusion neutrons was 18%. This detector played a complementary role in the experiment. Being fast and without any dead time after the muon stop, the neutron detector was used to measure the initial part of the time distributions of the fusion events in the 0.4 μs interval after the muon stop which was not accessible to the IC because of pile up between the fusion signals with the preceding muon signals. In addition, it defined the «zero time» in the time distributions measured with the IC. Figure 2 shows also the muon beam telescope consisting of two thin plastic counters (S1 and S2) in coincidence and a collimator (C) with a 2 cm^2 hole in the centre.

2.2. Hydrogen Ionization Chamber. The cryogenic hydrogen ionization chamber was designed and manufactured at PNPI. It is a gridded ionization chamber with the cathode-to-grid and grid-to-anode distances of 12.5 and 1.0 mm, respectively. The grid wires are 25 μm in diameter, and the wire pitch is 200 μm. The anode has a multi-pad structure as shown in Fig. 3. The central pads (B_1–B_5) define the useful muon stop area of 25×40 mm. It is surrounded by three veto pads (A_1–A_3) and by five entrance pads (C1–C5). The total anode area is 41×63 mm. The grid area is 60×75 mm, and the cathode is a disc of 110 mm in diameter. Such a geometry provides a uniform electric field in the cathode-grid space over the anode pads.
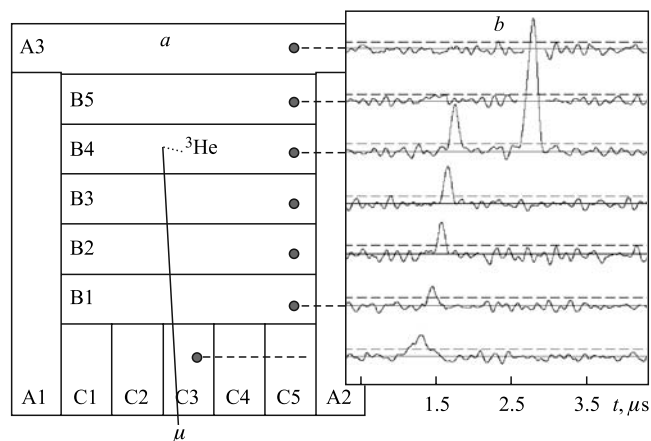

Fig. 3. *a*) The geometrical layout of the IC anode pads. *b*) Digitized FADC signals from the IC anode pads showing an example of a dd fusion event

The IC operates as a time-projection chamber. Muons enter the chamber nearly parallel to the electrode surface and stop in the space between the cathode and the grid. The ionization electrons drift towards the grid and are collected on the anode pads. Each anode pad had independent electronics and amplifier circuits. For signals above 120 keV, the anode signal was digitized by 8-bit flash ADCs for a period of 10 μs and recorded by the computer. The signal shape analysis provided the arrival front edge time T_μ^{FE}, the descending edge time T_μ^{DE} and the charge integral (proportional to the deposited energy) of each signal. The fusion signals are detected similarly. As an example, Fig. 3 shows a sequence of signals on the pads C_3–B_1–B_2–B_3–B_4 produced by a muon stopped at pad B_4 and followed by a fusion signal on the muon-stop pad.

The arrival times are measured with respect to the muon trigger time provided by the beam telescope $S1 \cdot S2$. The muon signal arrival time $T_\mu = (T_\mu^{\mathrm{FE}} + T_\mu^{\mathrm{DE}})/2$ on the muon-stop anode pad determines the vertical coordinate of the muon stop in the cathode-grid space: $z = T_\mu/W$, where W is the electron drift velocity. The time difference $T_{\mathrm{IC}} = T_f - T_\mu$ (where T_f is the arrival time of the fusion signal on the muon-stop anode) is used to determine the fusion time after the muon stop.

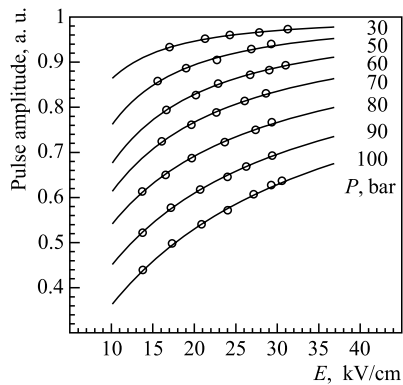The IC is designed to work at hydrogen gas pressures up to 120 bar. At such gas pressures, the electron–ion recombination of the initial ionization becomes essential. Figure 4 displays the results of special measurements of the recombination of the ionization produced by 4.78 MeV U-234 α particles in D_2 gas at various pressures. One can see that the recombination at high gas pressures cannot be eliminated completely, even applying the highest achievable electric fields (30 kV/cm in our case). However, as was shown in preliminary studies and confirmed by the present experiment, even considerable losses of the ionization charge due to recombination (30–40% of the initial charge) do not deteriorate seriously the energy resolution. Recombination just shifts the energy peaks without much distortion of their shapes. Therefore, complete elimination of the recombination is not needed. Moreover, the recombination effect proved to be even useful, as it allows to separate the ^{3}He and ^{3}Heμ peaks thus providing a unique method for measuring the muon sticking probability. Note that the singly charged ^{3}Heμ particles have a factor of three longer range than the doubly charged ^{3}He particles, and, as a consequence, the ionization charges produced by the ^{3}Heμ particles suffer much less recombination effect. Most of the mea-

Fig. 4. Dependencies of electron–ion recombination on electric field at various gas pressures

surements in the present experiment were performed at around 45 bar pressure (measured at room temperature) with about 16 kV/cm electric field in the IC drift zone and 30 kV/cm in the grid-anode space. Under these conditions, the recombination effect for ^{3}He (0.82 MeV) and ^{3}Heμ (0.80 MeV) particles was 30 and 10%, respectively.

Figure 5 shows the electron drift velocities measured in D_2 and H_2 gases at various pressures at room temperature. One can see that the drift velocity is determined by the ratio E/P of the electric field to the gas pressure. In our experiment, the drift velocity was around 0.7 cm/μs in the drift zone and 1.0 cm/μs in the grid-anode zone. The maximal collection time of the ionization electrons was 2.0 μs. As we observed in the present experiment, the drift velocity at a given ratio E/P is not changed noticeably in the explored temperature range 30–300 K under condition that the gas density is constant.

Fig. 5. Electron drift velocities in protium and in deuterium versus ratio of electric field (E) to gas pressure (P)

2.3. Cooling and Gas System. The experiment required that the IC temperature could be fixed at any point in the explored temperature range, stabilized and measured with absolute precision better than ± 0.5 K. To meet this requirement, a special cooling and temperature control system has been developed at PNPI which was able to stabilize the IC temperature with absolute precision ± 0.15 K in the temperature range from 28 to 350 K.

The IC engineering design had some specific features dictated by the conditions of our experiment. A critical part was the high-voltage input connector which could operate at pressures up to 120 bar in the hydrogen atmosphere gas, transmit the high voltage up to 40 kV without microdischarges and allow the temperature variations from 30 to 400 K[1]. Some precautions were taken in the choice of materials. The grid in the IC was made of gold plated tungsten wires soldered on a Kovar frame to keep the wire tension in the acceptable limits during the cooling procedure. Our experiment used hydrogen gas with various relative concentrations of molecular species including pure HD gas. To keep these concentrations stable during the run, one should exclude materials, like Ni, which may catalyze dissociation of the HD molecules. The Kovar grid frame proved to be such a catalyzer, but this effect was eliminated after the frame was covered

---

[1]Manufactured by SVETLANA company in St. Petersburg.

with an electrodeposited layer of silver. The final tests of the chamber filled with the HD gas showed that the HD concentration remained stable within 0.5% during at least several days.

Figure 6 presents the IC layout. The IC was mounted with a cooling jacket inside a high-vacuum vessel to allow cooling of the chamber and high-voltage supply to the cathode and to the grid of the ionization chamber. The vacuum in the vessel was about 10^{-7} mbar at room temperature and lower under cooling

Fig. 6. Layout of the cryogenic hydrogen ionization chamber

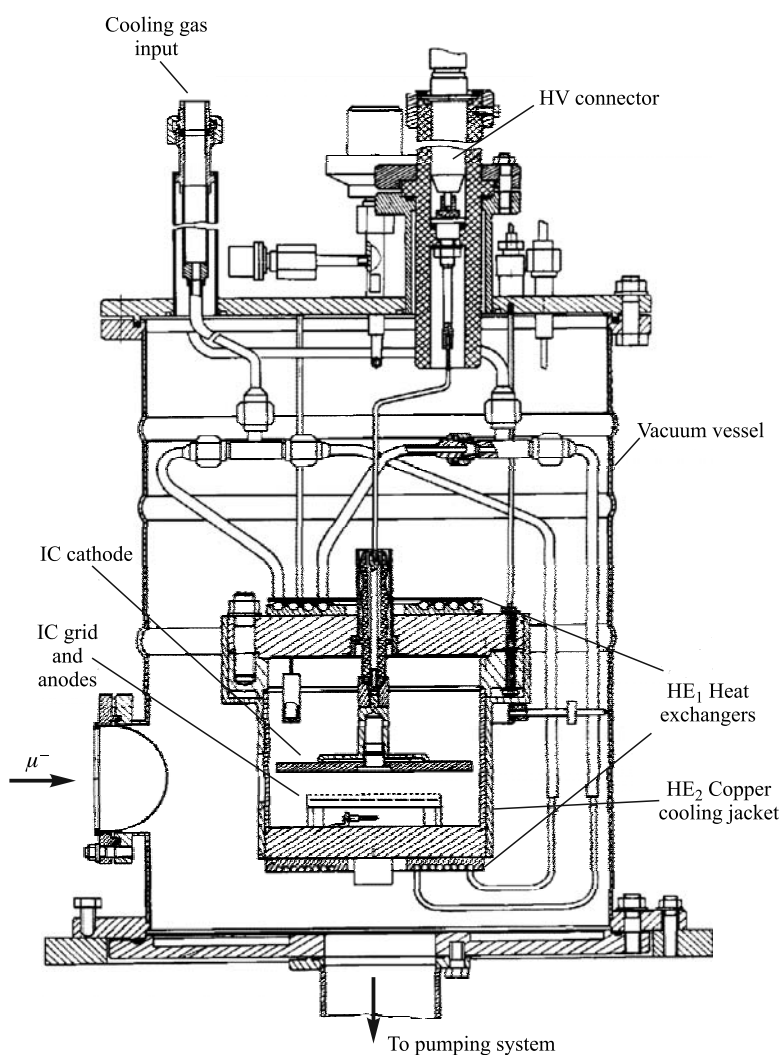conditions. The chamber body was a stainless steel cylinder 126 mm in diameter and 100 mm in height with 6 mm wall thickness. The thickness of the stainless steel top and bottom flanges was 18 mm. The muons entered the chamber through a 4 mm thick 25 mm in diameter beryllium window. The IC volume was 1.2 l.

The chamber was cooled with two liquid helium heat exchangers HE_1 and HE_2 which had direct thermal contact with the top and bottom chamber flanges. The principal scheme of the cooling system is presented in Fig. 7. The temperature of both IC flanges was measured with two platinum thermometers $PT100_1$ and $PT100_2$ specially calibrated in the temperature range 12–330 K with absolute precision ± 0.01 K. The liquid helium flux was regulated and stabilized by the pressure in the helium tank, the pressure being measured with a reference pressure sensor. The outlet helium gas was heated to room temperature in a heater, and its flux was controlled by the mass-flow controllers CV1 (at $T \leqslant 70$ K) or CV2 (at $T \geqslant 70$ K).
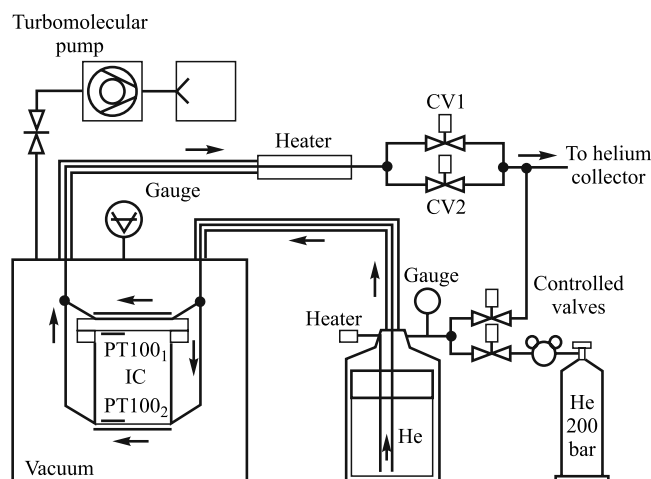
Fig. 7. Scheme of the ionization chamber cooling system

Besides cooling, the heat exchanger could be heated by electric currents with controllable power dissipation. In the experiment, both systems operated simultaneously. The heating system, being much less inertial, reduced considerably the setting time to the required temperature. The temperature setting procedure starts with a helium flux slightly higher than needed for the given temperature, the cooling power excess being compensated by heating. Then, knowing the introduced heating power, a correction for the helium flux was applied with corresponding reduction of the heating power. Finally, the heating system was used for the fine tuning and stabilization of the required temperature. The whole process was completely automated with a microprocessor and a PC. The allowed maximal rate

of the temperature change was set to be 5 K per minute, and the temperature difference between the top and bottom flanges during the temperature setting procedure did not exceed 3 K. With these limitations, the time required to reach the preset temperature and to stabilize it within ± 0.15 K was about 2 h.

The ionization chamber was filled with highly purified gases (D_2, HD, or $H_2 + D_2$) at 45 to 78 bar pressure at 300 K. The minimal pressure was about 4 bar at 30 K. The pressure was measured with three digital manometers with pressure ranges up to 100 bar (0.2 bar precision), up to 50 bar (0.1 bar precision), and up to 20 bar (0.02 bar precision). Purification of the D_2 and H_2 gases was performed using a specially constructed purification system. This system included a set of purification columns with Zeolite (CaA) operating at LN_2 temperature. The hydrogen purity was controlled by a chromatograph with a sensitivity at the 10^{-8} level for N_2 and O_2. Some measurements were performed with the $H_2 + D_2$ gas mixture both in the equilibrium and also in the nonequilibrium states. The equilibrium $H_2 + 2HD + D_2$ mixture was obtained using a column with Ni catalyzer. The $H_2/D_2/HD$ concentrations were measured with a chromatograph and with a mass-spectrometer at 1% level accuracy. A special setup was constructed for production of pure HD gas in the reaction $LiD + H_2O \rightarrow LiOH + HD$. The achieved concentration of the HD molecules in the gas was 97% with only 1% admixture of D_2 and 2% admixture of H_2.

3. MEASUREMENTS AND DATA PROCESSING

The experiments were carried out in the μE4 area at PSI with a muon beam having a beam spot 40×25 mm FWHM, $p_\mu = 40-50$ MeV/c, $\Delta p_\mu/p_\mu = 4\%$ FWHM and an intensity of 25 kHz. The measurements were performed at various temperatures with pure D_2 gas (16 runs), with equilibrated $H_2 + 2HD + D_2$ (4 runs) and nonequilibrated $H_2 + D_2$ (3 runs) gas mixtures, and with HD gas (3 runs). Typical running times were 20–30 h per temperature point. The strategy of the experiment was to select a clean sample of muon stops in the IC fiducial volume, to ensure close to 100% efficiency in detection of the dd fusion events, and to provide energy and time distributions of the fusion events measured with the IC for physics analysis.

3.1. Event Triggers. The first-level trigger

$$\mathrm{Tr}\,1 = \mathrm{S1} \cdot \mathrm{S2} \cdot \overline{\mathrm{S1}(-7\ \mu\mathrm{s} + 9\ \mu\mathrm{s})} \tag{7}$$

identified muons within the beam telescope acceptance (2 cm^2) with an additional requirement that there should be no other muons detected by the S1 counter (area of 15×15 cm) in the time interval from 7 μs before and 9 μs after the S1·S2 signal. The second-level trigger used the signals from the B anodes which had two charge-integrating trigger circuits with the «E_{low} threshold» at 120 keV and

the «E_{high} threshold» at 800 keV. The energy resolution was 30 keV (σ). The logic scheme provided three triggering modes:

(i) E_{low} trigger. A low threshold signal during the first 2 μs (maximal drift time) on at least one B anode signaling an incoming muon.

(ii) $E_{\text{low}} \cdot E_{\text{low}}$ trigger. Two separate low threshold signals ($\Delta t \geqslant 0.3$ μs) within 10 μs on the same B anode indicating a muon stop followed by a fusion event separated in time.

(ii) E_{high} trigger. A signal on any B anode above the E_{high} threshold indicating a $(p + t)$ event or a ^{3}He signal piling up with the muon signal.

The muon stops, selected by the E_{low} trigger, were prescaled by a factor P_s equal to 100, 50 or 20 depending on the fusion probability per muon stop. Summarizing, the final trigger was

$$\text{Tr}\,2 = \text{Tr}\,1 \left(\frac{E_{\text{low}}}{P_s} + E_{\text{low}} \cdot E_{\text{low}} + E_{\text{high}} \right). \tag{8}$$

At typical run conditions, the Tr 1 rate was ~ 2 kHz, while the rate of Tr 2 was about 20 Hz.

3.2. Muon Stop Selection. First, the B anode which detected the muon stop was identified. In the case of the $E_{\text{low}} \cdot E_{\text{low}}$ trigger and the E_{high} trigger, the muon-stop B anode is just the anode producing the corresponding trigger, for the E_{low} trigger, it was the most downstream B anode along the muon track.

The arrival time T_μ of the muon signal from the muon-stop anode relative to the TR1 signal was measured, and it was required that there should be no signals on the A$_1$–A$_3$ anodes within the time interval of ± 50 ns. This restricted the penetration of the muon tracks into the A anodes region to a small boarder region of 0.3–0.4 mm where stopping muons produce signals below the thresholds in the A anode channels. The vertical fiducial volume was determined by cuts on the drift times T_μ to the muon-stop B anode (Fig. 8) so that only muon stop at
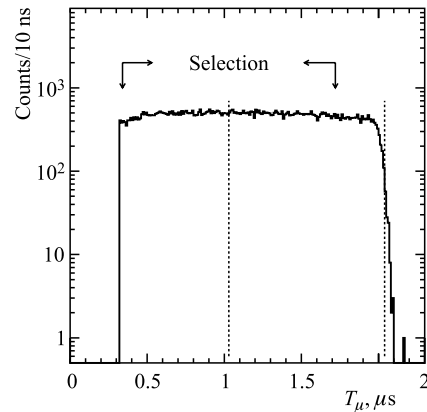

Fig. 8. Distribution of mean times T_μ of the muon signals on the muon-stop B anodes. The two dashed lines correspond to the muon stops in the middle of the space between the grid and the cathode and to those close to the cathode position. The muon stops close to the grid ($T_\mu \leqslant 0.3$ μs) were rejected on trigger level

least 1.5 mm away from the cathode and from the grid were accepted, such that the ^{3}He, ^{3}Heμ and triton tracks would not reach the electrodes. The energy of the muon stop was selected based on the combination $S = E_i + 2E_{i-1}$, where E_i is the energy signal on the muon-stop B anode; and E_{i-1}, the one on the preceding B anode. Figure 9 demonstrates that the S distributions of the muon signals detected with the E_{low} and the $E_{low} \cdot E_{low}$ trigger both exhibit a sharp peak at $S = 1.15$ MeV corresponding to undisturbed muon signals. A small peak at $S = 1.75$ MeV is due to pile up of the ^{3}He signals with the muon signals. Piling up with the $(t + p)$-signals shifts the muon signals to $S > 2$ MeV (not seen in Fig. 9). Both S distributions are identical except for the low energy noise contribution to the E_{low} trigger events. In the analysis, the selected S region was $0.83 < S < 1.44$ MeV. This cut is loose enough to provide equal efficiencies within better than $\pm 0.1\%$ for muon registration in both trigger modes. This allows one to use the E_{low} trigger events for controlling the detection efficiency in the $E_{low} \cdot E_{low}$ mode and also for absolute calibration of the measured fusion rates.
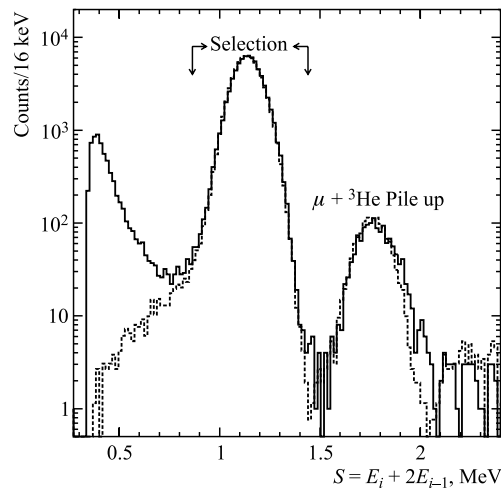
Fig. 9. The S distributions of the muon signals. E_i and E_{i-1} are the energy deposits on the muon-stop B anode and on the preceding anode, respectively. The arrows indicate the region of the muon-stop selection. The solid and dashed lines correspond to the muon signals detected with the E_{low} trigger and with the $E_{low} \cdot E_{low}$ trigger, respectively

Our main event trigger ($E_{low} \cdot E_{low}$) required muon stop and fusion signals from the same B anode. This caused a class of events escaping triggering, i.e., muons which intruded so little into the anode region that the created charge signal remained below threshold. This class was carefully reconstructed using the E_{low} trigger events. A correction on a level of 3–7% with systematic uncertainty

$\pm 0.7\%$ was applied to compensate for these losses. The absolute calibration of the fusion rates was based on the number of the muon stops in the E_{low} trigger events selected by the S cuts as shown in Fig. 9. This number does not include the muon-fusion pile up events which may constitute 2–5% of the total number of the muon stops. This correction could be precisely determined from the time distribution of fusion events.

In conclusion, clean muon stops were selected in the fiducial volume well isolated from the chamber electrodes, and the absolute number of the selected muon stops was controlled to better than 1% precision. The typical rate of the clean muon stops was ~ 100 Hz of the ~ 2 kHz Tr 1 rate and $2 \cdot 10^6$ to $45 \cdot 10^6$ clean muon stops were collected per run, depending on the run conditions.

3.3. Energy Distributions of dd **Fusion Events.** Figure 10 shows a typical energy spectrum measured in pure D_2 gas at 120.3 K (the gas density was 5% of the liquid hydrogen density LHD defined as $4.25 \cdot 10^{22}$ nuclei/cm^3). This spectrum corresponds to the first fusion signals arriving after the muon signals integrated over the 0.5–7.5 μs time interval. The energy of the fusion signals is the sum of the integrated charges on the muon-stop B anode with those on the neighbor B or A anodes closest to the muon-stop anode within a ± 50 ns coincidence.
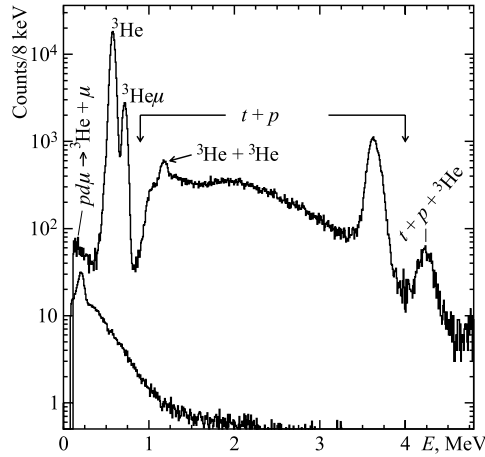
Fig. 10. Energy spectrum of fusion events in D_2 gas at $T = 120.3$ K integrated over 0.5–7.5 μs time interval. The dashed histogram corresponds to the μ-capture background measured in $H_2 + N_2(140$ ppm) gas mixture at $T = 300$ K and normalized to the energy region 0.1–0.45 MeV

One can distinguish the following components. The ^{3}He peak at 0.58 MeV corresponds to the fusion channel $dd \rightarrow {}^3\text{He} + n$ (initial energy $E_0({}^3\text{He}) = 0.82$ MeV, track length $\mathcal{L}({}^3\text{He}) = 0.26$ mm). The ^{3}Heμ peak at 0.72 MeV

corresponds to the fusion channel $dd \rightarrow {}^3\mathrm{He}\mu + n$ ($E_0({}^3\mathrm{He}\mu) = 0.80$ MeV, $\mathcal{L}({}^3\mathrm{He}\mu) = 0.6$ mm). The continuous distribution from 0.9 to 4 MeV corresponds to the fusion channel $dd \rightarrow t + p$ ($E_0(t) = 1.01$ MeV, $E_0(p) = 3.02$ MeV, $\mathcal{L}(t) = 1$ mm, $\mathcal{L}(p) = 17.2$ mm).

The events below 3.6 MeV down to 1 MeV are due to proton tracks escaping the sensitive volume defined by the two neighbor anodes. The minimal energy in the $(t + p)$ distribution is determined by the energy of the triton which never escapes the sensitive volume. Two small peaks in Fig. 10 originate from piling up of the second and the first fusion signals: the $({}^3\mathrm{He} + {}^3\mathrm{He})$ pile up peak at 1.2 MeV and the $(t + p) + {}^3\mathrm{He}$ peak at 4.2 MeV. The observed peak energies are shifted with respect to the initial energies due to the charge recombination effect.

The events below 0.45 MeV are due to two background reactions: pd fusion and muon capture on gas impurities. The pd fusion occurs due to a small hydrogen admixture in deuterium (in the D_2 runs the admixture of HD molecules was 0.6% according to the chromatographic analysis) with the two channels $pd \rightarrow {}^3\mathrm{He}\,(0.2 \text{ MeV}) + \mu\,(5.3 \text{ MeV})$ and $pd \rightarrow {}^3\mathrm{He}\mu + \gamma$ (5.5 MeV). The 0.2 MeV ${}^3\mathrm{He}$ particles from the first channel are detected producing a peak just above the 120 keV registration threshold with a small tail towards higher energy due to partial absorption of the 5.3 MeV muon energy. This tail ends at 0.4 MeV well below the region where the dd fusion products are detected. The second channel of the pd fusion is not directly detected because the ${}^3\mathrm{He}\mu$ energy is below our threshold. Thus, pd fusion does not produce any background interfering with the dd fusion events, but we determined this background and subtracted it from the spectrum for energies $\leqslant 0.40$ MeV. The remaining events in this region are due to nuclear muon capture on impurities and can serve as an absolute calibration of this capture background. The shape of the $pd \rightarrow {}^3\mathrm{He} + \mu$ peak was measured in our HD experiment (see Fig. 14 in Subsec. 4.1) and its detection efficiency determined to be $\varepsilon_{pd} = 85\%$. Knowing $\lambda_{pd\mu}(T)$, C_p, and ε_{pd}, the pd background for each D_2 run could be evaluated. Moreover, in some D_2 runs with exceptionally low nitrogen concentration it was possible to determine the C_p directly. The results ($C_p = 0.2{-}0.3\%$) were in agreement with the chromatographic data. The energy distribution of the μ-capture events was measured in a special run with the gas mixture $H_2 + N_2$ (140 ppm) at 45 bar pressure at room temperature and the efficiency for detecting μ-capture events was determined as $\varepsilon_r = 0.55$. Figure 10 presents the energy distribution of the μ-capture events normalized to the yield of these events in the energy region 0.1–0.45 MeV measured in the D_2 run at 120.3 K. For the data of H/D runs, where the low energy region contains significant pd fusion signals, this normalization was checked with the pure HD measurement. There the pile up probability of two dd fusion signals was extremely low, so that the capture events could be normalized to the high energy (> 5 MeV) part of the spectrum (see Fig. 14).

Based on the number of the μ-capture events N_{cap} and assuming the gas impurity to be nitrogen, one can calculate the muon transfer rate Λ_{dZ} and the concentrations C_Z in each run using an approximate relation:

$$\Lambda_{dZ} = \varphi \lambda_{dZ} C_Z = N_{cap} \frac{\langle \Lambda_{dd\mu} \rangle + \lambda_0}{N_\mu \varepsilon_r \lambda_c / (\lambda_0 + \lambda_c)}, \qquad (9)$$

where $\lambda_{dZ} = 1.45 \cdot 10^{11}$ s^{-1} [42] is the muon transfer rate normalized to liquid hydrogen density LHD, $\lambda_c = 0.057$ μs^{-1} is the muon capture rate in nitrogen, φ is the gas density normalized to LHD, ε_r is detection efficiency of the muon capture reaction, $\langle \Lambda_{dd\mu} \rangle$ is the *integral* $dd\mu$ formation rate determined approximately by the ratio of the detected fusion events N_f to the number of the selected muon stops N_μ: $\langle \Lambda_{dd\mu} \rangle = \lambda_0 N_f / (N_\mu - N_f)$.

3.4. Time Distributions of dd Fusion Events. To study the time distribution of the dd fusion events, we have selected the ^{3}He and ^{3}Heμ events, that is, the events in the energy range from 0.4 to 0.8 MeV (Fig. 10). This choice has the following advantages: The short track length of ^{3}He and ^{3}Heμ particles leads to short duration of the signals ($\leqslant 200$ ns) and, as a consequence, to a minimal dead time after muon signals. The short duration of these signals makes them similar in shape to the muon signals (note that muon tracks are nearly parallel to the grid surface). This facilitates precision measurement of the time difference between the fusion and muon signals. Because the pile up probability of the (^{3}He + ^{3}Heμ) signals with the next fusions is similar to that of the muon signals, the overall correction for normalizing the (^{3}He + ^{3}Heμ) time distributions is strongly reduced compared with the case of the $(t + p)$ time distributions. The ^{3}He + n fusion channel can be simultaneously detected by the neutron detector to determine the time zero of the ^{3}He time distribution measured with the ionization chamber.

The fusion time T_{IC} was determined as the difference between the mean time of the ^{3}He (^{3}Heμ) signal and the mean time of the muon signal, $T_{IC} = T_f - T_\mu$, both signals detected on the muon-stop B anode. With this measuring technique, slight asymmetries of the muon entrance distribution may cause some systematic shifts of the T_{IC} timing. This effect was carefully evaluated by comparison with the fusion time T_N of the same event measured with the neutron detector: $T_N = t_n - t_n^0$. Here t_n is the time of a neutron hit in one of the neutron counters correlated with the ^{3}He (^{3}Heμ) signal in the IC and t_n^0 is the «time zero» in the neutron time distribution. The value of t_n^0 was determined with precision better than ± 1 ns by the front edge (half-maximum) of the time distribution of dd fusion neutrons in pure HD gas, where the dd fusions process starts immediately after the muon stop (see Subsec. 5.3). If compared with the «time zero» t_e^0 for time distribution of electrons from μ^- decay (Fig. 11), the neutron «time zero» t_n^0 was shifted by 12 ns, which reflects the mean time of flight of the 2.45 MeV neutrons
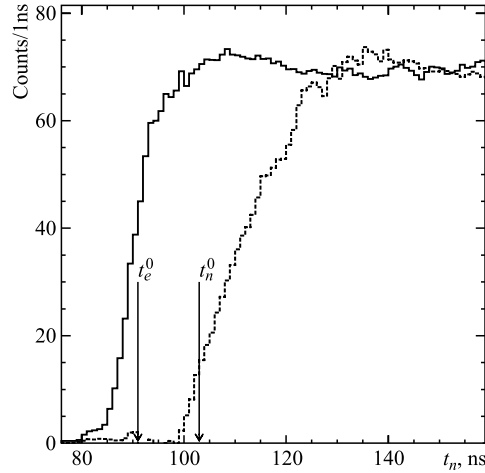
Fig. 11. Initial parts of time distributions of electrons from μ decay (solid line) and neutrons from dd fusion (dashed line) measured by the neutron detectors. The half-maximum of the electron time distribution determines the «time zero» t_e^0 for electrons. The value t_n^0 is the «time zero» for 2.45 MeV dd fusion neutrons determined by the front edge (half-maximum) of the time distribution of dd fusion neutrons in pure HD gas (see text). The difference in rise times of the electron and neutron distributions is due to thermalization time of $d\mu$ atoms in D_2 gas. The difference $t_n^0 - t_e^0 = 12$ ns reflects the mean time of flight of the 2.45 MeV neutrons before absorption in the scintillators

before absorption in the scintillators. The relatively slow rise of the neutron time distribution shown in Fig. 11 is due to the thermalization time of $d\mu$ atoms in D_2 gas. The measured difference $\Delta T = T_{IC} - T_N$ in Fig. 12 is taken as a correction to the time measured by the IC. This correction for different runs varied from -9 to $+2$ ns. Taking into account possible systematic errors, we concluded that the «time zero» in the time distributions measured with the IC was known with precision ± 2 ns limiting this error source in measurements of $\lambda_{dd\mu}^{3/2}$ to $\pm 0.4\%$. For simplicity, we shall use further the notation $T_{IC} \equiv t$.

Figure 13 presents the time distribution of the ^{3}He $(^3$He$\mu)$ events measured with the IC at 120.3 K. The drop in the IC spectrum at $t \leqslant 0.4$ μs is due to piling up of the fusion signals on the muon signals. The neutron time distributions were measured in coincidence with all ^{3}He $(^3$He$\mu)$ events including the pile up events. This yielded the time spectrum starting from $T_N = 0$. Both the IC and the neutron time spectra clearly show the two-exponential shape first observed in [16]. These spectra contain information on the $dd\mu$ formation rates $\Lambda_{dd\mu}^{3/2}$, $\Lambda_{dd\mu}^{1/2}$ and on the spin flip rate Λ_{21}, which will be analyzed in Subsubsec. 4.3.1.
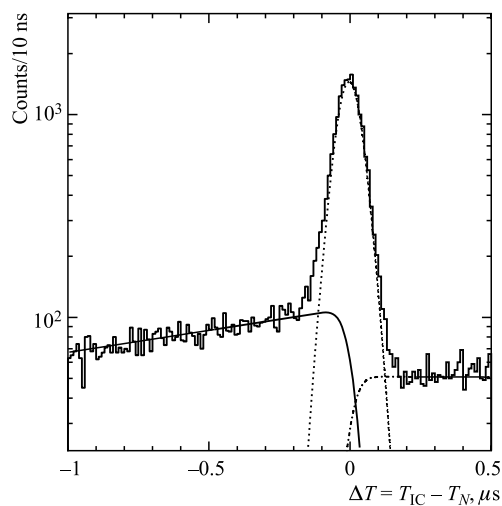
Fig. 12. Time correlation between fusion signals from the IC and those from the neutron detectors. The left-side tail is due to accidentals with the μ-decay electrons produced after the dd fusion and registered by the neutron detector. The mean value of ΔT is determined by the maximum of the Gaussian fitted to the distribution
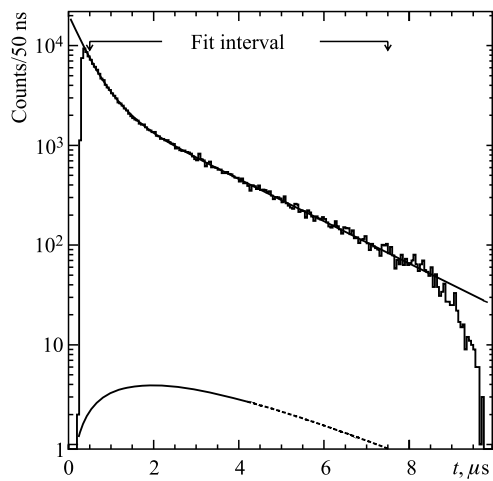
Fig. 13. Time distribution of ^{3}He and ^{3}Heμ events in D$_2$ gas measured with the IC at $T = 120.3$ K. The dashed line corresponds to the μ-capture background. The solid line is the result of the fit

In our main analysis, we used the IC time distributions as they provided higher statistics, better precision in absolute normalization, and low background if compared with the neutron time spectra. The only background correction required is due to muon capture on gas impurities. Following the kinetics scheme (Fig. 1), the time distribution of the μ-capture events can be calculated once the impurity concentration assumed to be N_2 is determined from Eq. (9). The integral of this spectrum should be normalized to the number of μ-capture events in the selected energy range under the ^3He ($^3\text{He}\mu$) peaks. This procedure was checked in the D_2 run at 50.2 K in which the N_2 concentration was very high (15 ppm). In that run, the time distribution was obtained of the μ-capture events selected in the range 0.1–0.4 MeV. It was shown that the calculated capture time distribution describes well the measured distribution. Moreover, the fit determined Λ_{dZ} and λ_c. The measured $\lambda_c = 0.057(6) \cdot 10^6$ s^{-1} proved to be in good agreement with the corresponding value known for nitrogen $\lambda_c(N_2) = 0.065(5) \cdot 10^6$ s^{-1} [43]. The background calculated in this way is indicated in Fig. 13. It became more important for higher levels of impurities and for lower dd fusion rates. However, in all cases the μ-capture background was under control and could not deteriorate the analysis precision. Other sources of background (double muon events, etc.) were negligible as was checked in a run with a μ^+ beam.

4. EXPERIMENTAL DATA AND ANALYSIS

4.1. Running Conditions. Tables 2 to 5 compile the experimental conditions and statistics collected in our measurements. As regards the ortho- and para-population of the D_2 molecules (compare the experimental studies of ortho-para effects [44]), the gas was filled as an «equilibrium gas mixture» corresponding to $T = 77$ K (the temperature of the Zeolite columns in the gas purification system). The measured ortho/para ratio at the exit of the purification system was $O/P = 2.4/1$ in agreement with the expected equilibrium ortho/para ratio at $T = 77$ K. During the gas filling, the IC was at room temperature. Thereafter, it was cooled to the lowest temperature and then the temperature was increased step by step from run 1 to run 3 in the D_2-94 experiment and from run 1 to run 12 in

Table 2. **Experimental conditions and statistics in experiment D_2-94**

Run	T, K	φ, %	N_μ, units of 10^6	N_{He}	N_{BG}	Λ_{dZ}, 10^6 s^{-1}	C_Z, ppm
1	51.0	5.05	12.9	156223	2343	0.0056	0.76
2	71.0	5.04	6.12	100648	1623	0.0054	0.74
3	96.0	5.02	3.29	79231	990	0.0057	0.78

Table 3. **Experimental conditions and statistics in experiment D_2-95**

Run	T, K	φ, %	N_μ, units of 10^6	N_{He}	N_{BG}	Λ_{dZ}, 10^6 s^{-1}	C_Z, ppm
1	50.2	5.13	5.83	82917	16574	0.116	15.6
2	32.2	5.14	3.77	63488	446	0.003	0.40
3	36.2	5.14	5.46	89116	7273	0.035	4.70
4	40.3	5.14	6.18	95896	13717	0.063	8.45
5	45.3	5.05	5.24	80633	71	0.0003	0.041
6	60.3	5.04	5.72	97437	142	0.00053	0.073
7	120.3	4.99	3.97	177023	365	0.0024	0.33
8	150.3	4.97	2.60	165676	349	0.0034	0.47
9	200.2	4.94	1.70	155290	256	0.004	0.56
10	250.1	4.89	2.54	270154	879	0.007	0.99
11	300.0	4.85	1.95	214643	985	0.012	1.71
12	350.0	4.81	2.04	192674	7902	0.093	13.3
13	28.3	2.76	3.54	63033	19	0.0002	0.05

Table 4. **Experimental conditions and statistics in experiment H_2/D_2-96. NE — non-equilibrium gas state ($H_2 + D_2$), EQ — equilibrium gas state ($H_2 + 2HD + D_2$)**

Run	T, K	φ, %	Gas	N_μ, 10^6	N_{He}	N_{BG}	Λ_{dZ}, 10^6 s^{-1}	C_Z, ppm
1	50.2	5.12	NE	19.5	290931	2491	0.0053(6)	0.71
2	150.2	5.02	NE	11.0	372245	1070	0.004(1)	0.55
3	300.2	4.97	NE	3.96	205744	117	0.0040(10)	0.56
4	50.2	5.07	EQ	34.1	309715	2987	0.0032(6)	0.44
5	100.2	5.00	EQ	15.6	202395	1393	0.0035(10)	0.48
6	150.2	4.97	EQ	18.9	371105	1744	0.0036(6)	0.50
7	300.2	4.91	EQ	5.56	166115	474	0.0043(9)	0.60

Table 5. **Experimental conditions and statistics in experiment HD-96**

Run	T, K	φ, %	N_μ, units of 10^6	N_{He}	N_{BG}	Λ_{dZ}, 10^6 s^{-1}	C_Z, ppm
1	300.3	4.87	25.9	73023	2102	0.0032	0.45
2	150.3	4.78	25.2	51575	1672	0.0027	0.39
3	50.2	4.74	45.8	60220	2903	0.0043	0.63

the D_2-95 experiment. The total running time was 6 days and 18 days in the D_2-94 and D_2-95 experiments, respectively. It is anticipated that the ortho/para ratio was unchanged during this time as there were no materials inside the chamber which could catalyze the ortho-para transitions. During the D_2-95 experiment the gas was refilled between run 4 and run 5, as the nitrogen contamination was too high caused by an error in the first gas filling procedure. The gas temperature was stabilized and measured in each run with absolute precision of ± 0.15 K. The gas pressure was measured with precision which varied from $\pm 0.5\%$ at $T = 30$ K (4 bar pressure) to $\pm 0.2\%$ at $T = 300$ K (45 bar pressure). Based on these measurements, the deuterium gas density normalized to LHD was calculated by applying the standard formula with a correction factor for the non-ideal gas: $\varphi = 0.341 P(1 - \xi P)T^{-1}$, where P is the gas pressure in bar, T is the temperature in Kelvin, $\xi(\mathrm{H}_2) = 5.9 \cdot 10^{-4}$ and $\xi(\mathrm{D}_2) = 5.6 \cdot 10^{-4}$. Summing up the possible errors in T, P and in the correction for the nonideal gas, we conclude that the deuterium density was determined with precision of $\pm 0.8\%$ at $T = 30$ K and $\pm 0.4\%$ or better at $T \geqslant 60$ K. Note that the gas densities presented in Tables 2 to 4 show some continuous decrease with increasing temperature due to the gas redistribution between the cooled IC volume and the gas filling tubes at room temperature.

The statistics collected in each run is illustrated in Tables 2 to 5 by the number of clean muon stops N_μ and by the number N_{He} of the corresponding (^{3}He $+ \, ^3$Heμ) fusion events. N_μ is defined as $N_\mu = N_\mu(P_s)P_s$, where $N_\mu(P_s)$ is the number of the clean muon stops in the E_{low} trigger with prescaling factor P_s. N_{He} is the number of the events in the energy range from 0.4 to 0.8 MeV (Fig. 10) after subtraction of the μ-capture background N_{BG}. This background, as well as the transfer rate to the impurity Λ_{dZ} and the impurity concentration C_Z were determined following the procedure described in Subsec. 3.3. The relative concentrations of the H_2, D_2, and HD molecules in H_2/D_2-96 and HD-96 experiments were measured with a gas chromatograph. The results are presented in Table 6.

Table 6. **Chromatographic data on H_2/HD/D_2 concentrations (in %) for experiments H_2/D_2-96 and HD-96**

Experiment	Run	C_{D_2}	C_{H_2}	C_{HD}
H_2/D_2-96	1–3	47.6	49.0	3.4
	4–7	25.7	26.6	47.7
HD-96	1	0.78	1.84	97.38
	2	1.02	2.07	96.91
	3	1.10	2.15	96.75

Examples of the measured energy and time distributions of dd fusion events are displayed in Fig. 14.
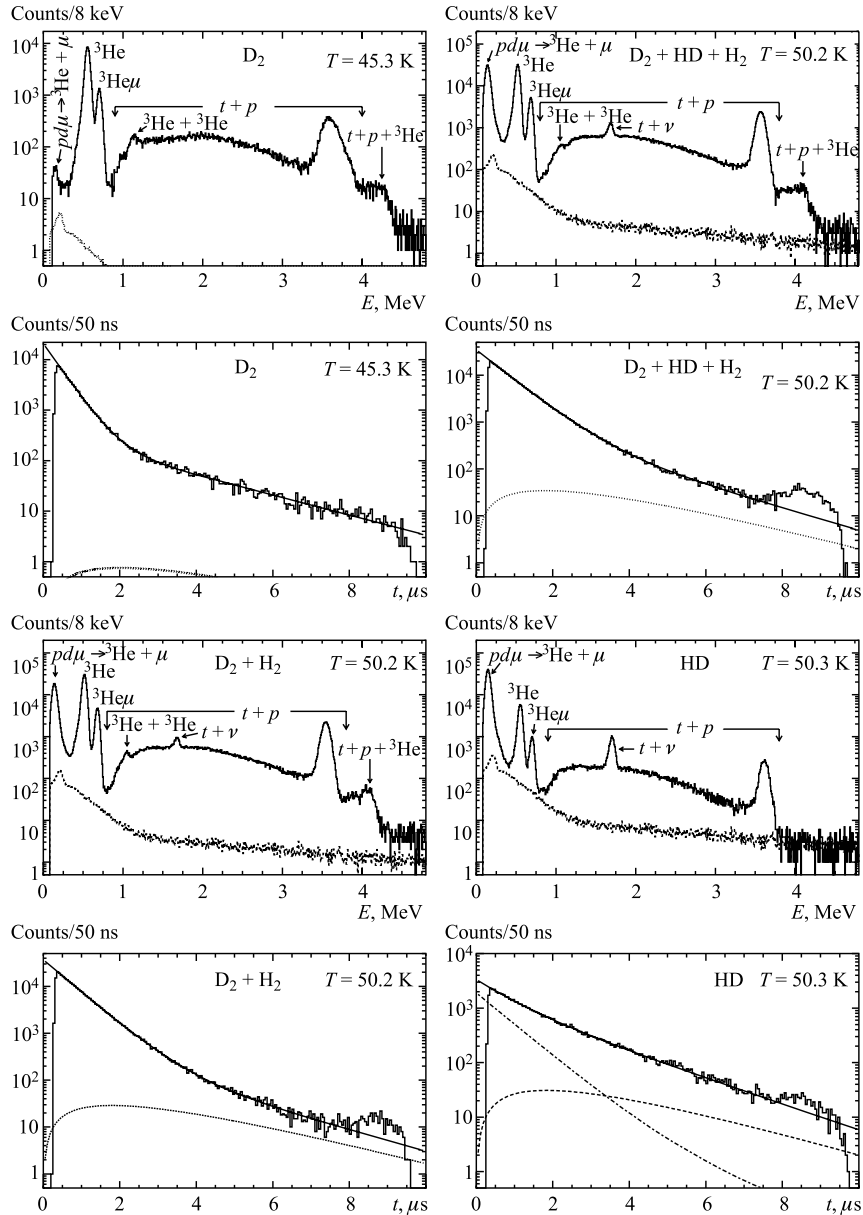
Fig. 14. Energy and time distribution of fusion events. The dashed histograms and lines correspond to the μ-capture background. The dash-dotted line in time distribution of fusion events in HD at 50.3 K represents dd fusions due to $d\mu$ collisions with D_2 molecules

4.2. Analysis of Fusion Energy Distributions. *4.2.1. Muon Sticking Probability.* The first measurement of the muon sticking probability in $dd\mu$ fusion in the Gatchina experiment [18] found a final sticking probability $\omega_d = 0.122(3)$ at $\varphi = 0.102$. In the present experiment, we used the same experimental method, however, with much higher statistics and measured ω_d in pure D_2 gas at room temperature at two deuterium densities $\varphi = 0.0485$ and $\varphi = 0.0837$. The difference in the recombination of the initial ionization produced in the IC by the singly charged $(^3He\mu)^+$ and doubly charged $(^3He)^{++}$ particles resulted in the separation of the ^3He and $^3He\mu$ peaks in the measured amplitude distributions of the fusion signals (see Fig. 15). To the right of the $^3He\mu$ the $(^3He + ^3He)$ pile up peak is seen. There is some background under the $^3He\mu$ peak from the neighbor peaks and also from the stripping events, that is from the events corresponding to the $^3He\mu$ particles which have lost the muon during deceleration. This background was eliminated by «the survived muon method». If fusion events followed by another fusion are selected, the muon could not remain stuck on the first ^3He, otherwise it could not have catalyzed the next fusion. Therefore, thus selected events will contain all the events as in the unselected spectrum except the final sticking events. We selected only the $(^3He + ^3He\mu)$ signals from the next fusion events which helped to eliminate some small background under the $^3He\mu$ peak caused by the $^3He\mu$ capture events which might simulate the next fusion. Figure 15 shows the survived muon spectrum normalized to the unselected spec-
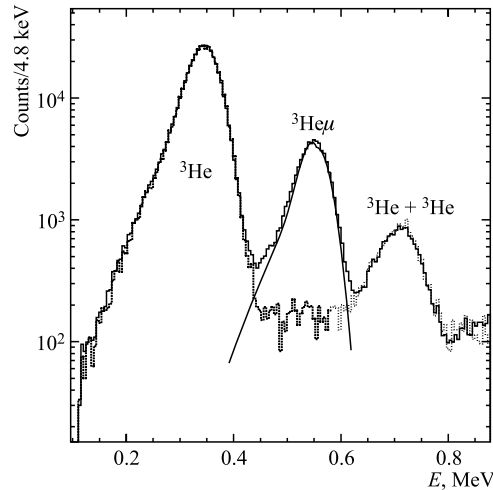

Fig. 15. Low energy part of the dd fusion energy distribution measured in D_2 gas at $T = 300$ K and $\varphi = 0.0837$. The dotted line shows the survived muon spectrum normalized to the unselected spectrum in the region of the ^3He peak. The difference between these two spectra determines the final muon sticking probability

trum in the region of the ³He peak. The difference between these two spectra in the region of the ³Heμ peak gives the number $N(^3\mathrm{He}\mu)$ with high precision. Then the final muon sticking probability is calculated as

$$\omega_d = \frac{N(^3\mathrm{He}\mu)}{N(^3\mathrm{He}\mu) + \dfrac{N(^3\mathrm{He})}{(1 - W_{\mathrm{pileup}})}}, \tag{10}$$

where $N(^3\mathrm{He})$ is the number of events in the ³He peak and $(1 - W_{\mathrm{pileup}})$ is the pile up correction that takes into account some reduction in $N(^3\mathrm{He})$ caused by piling up of the second fusion signals on the ³He signals. For $N(^3\mathrm{He}\mu)$ there is no subsequent fusion. $W_{\mathrm{pileup}} = 0.075(1)$ at $\varphi = 0.0837$ and $W_{\mathrm{pileup}} = 0.050(1)$ at $\varphi = 0.0485$ were calculated from the measured time distributions between the first and second fusions. The following final sticking probabilities were obtained

$$\omega_d = 0.1224(6) \quad \mathrm{at} \quad \varphi = 0.0837 \ \mathrm{and}$$
$$\omega_d = 0.1234(7) \quad \mathrm{at} \quad \varphi = 0.0485 \tag{11}$$

in agreement with the earlier, but less precise result [18].

4.2.2. Branching Ratios of dd Fusion Channels. From the data of the D₂ experiment, we have determined the ratio $R = Y(^3\mathrm{He} + {}^3\mathrm{He}\mu)/Y(t + p)$ using the amplitude distributions of the fusion signals in the steady-state region within $2 \leqslant t \leqslant 7.5$ μs (see Fig. 16). This time window avoids the steep slope in the time spectrum to reduce the time smearing correction to the yield of $(t + p)$ events
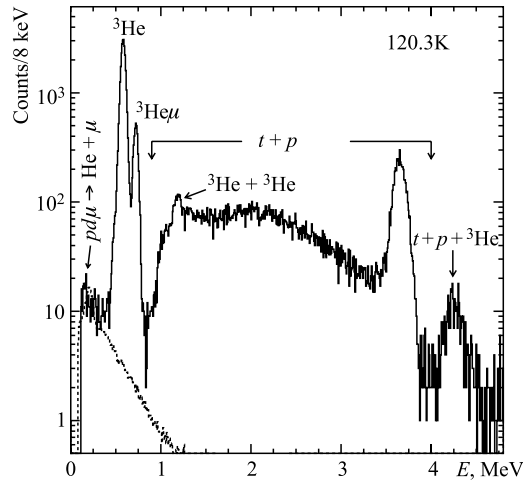

Fig. 16. Energy spectrum of *dd* fusion events for the steady-state time region ($t > 2$ μs). The dashed histogram corresponds to the μ-capture background

created by long proton tracks. Those shift the measured time distribution towards larger times and, as a consequence, increase the number of the $(t + p)$ events detected in the selected time window. The yields were determined taking into account several corrections.

$$Y(^3\text{He}+^3\text{He}\mu) = [N(^3\text{He}+^3\text{He}\mu)-N_{\text{BG}}(^3\text{He}+^3\text{He}\mu)](1-\varepsilon_{\text{tr}})+N_{\text{pileup}}, \quad (12)$$

$$Y(t + p) = [N(t + p) - N_{\text{BG}}(t + p)]\varepsilon_{\text{sm}} - N_{\text{pileup}}. \quad (13)$$

Here $N(^3\text{He}+^3\text{He}\mu)$ is the total number of events and $N_{\text{BG}}(^3\text{He}+^3\text{He}\mu)$ is the number of background capture events in the energy range 0.4–0.8 MeV, while $N(t + p)$ is the total number of events and $N_{\text{BG}}(t + p)$ is the number of capture background events in the energy range 0.8–8 MeV. N_{pileup} is the number of pile up events, ε_{tr} is the correction for trigger losses of ^{3}He fusions close to the edges of the anodes, ε_{sm} is the proton smearing correction. The μ-capture background was calculated as described in Subsec. 3.4. The background corrections for both fusion channels proved to be nearly equal, so that the overall correction to the ratio R was less than 1%. N_{pileup} takes into account the ^{3}He events that were transferred from the ^{3}He peak to the $t + p$ region because of pile up with the second fusion. This correction, calculated in a similar way as explained in Subsubsec. 4.2.1, ranged from 5 to 10%. There is no pile up correction for a

Table 7. $dd\mu$ **formation and spin flip rates** (10^6 **s**$^{-1}$**), and branching ratios in pure** $\mathbf{D_2}$ **gas**

| T, K	φ, %	$\widetilde{\lambda}_{dd\mu}^{1/2}$	$\widetilde{\lambda}_{dd\mu}^{3/2}$	$\widetilde{\lambda}_{dd\mu}$	$\widetilde{\lambda}_{21}$	R
28.3	2.76	0.053(3)	3.98(5)	0.053(3)	37.0(4)	—
32.2	5.14	0.051(1)	4.13(7)	0.051(1)	37.1(3)	1.07(3)
36.2	5.14	0.049(2)	3.96(6)	0.049(2)	36.6(2)	—
40.3	5.14	0.050(fix)	3.88(6)	—	36.6(2)	—
45.3	5.05	0.0515(8)	3.92(6)	0.0515(8)	36.8(3)	1.03(3)
50.2	5.13	0.0544(fix)	3.90(6)	—	35.9(3)	—
51.0	5.05	0.0537(7)	3.79(4)	0.0538(7)	35.77(16)	1.05(1)
60.3	5.04	0.063(1)	3.89(6)	0.0637(10)	36.04(25)	1.08(2)
71.0	5.04	0.088(1)	4.05(5)	0.091(1)	35.38(25)	1.24(1)
96.0	5.02	0.246(3)	4.42(7)	0.270(3)	34.8(4)	1.34(1)
120.3	4.99	0.528(4)	4.98(10)	0.609(4)	35.0(5)	1.40(1)
150.3	4.97	0.943(5)	5.07(15)	1.129(8)	35.9(9)	1.43(1)
200.2	4.94	1.65(2)	4.59(15)	1.97(2)	34.2(1.5)	1.40(1)
250.1	4.89	2.202(27)	4.28(12)	2.56(3)	37.0(2.0)	1.42(1)
300.0	4.85	2.549(23)	3.75(fix)	—	—	1.44(1)
350.0	4.81	2.70(5)	3.28(fix)	—	—	1.44(1)
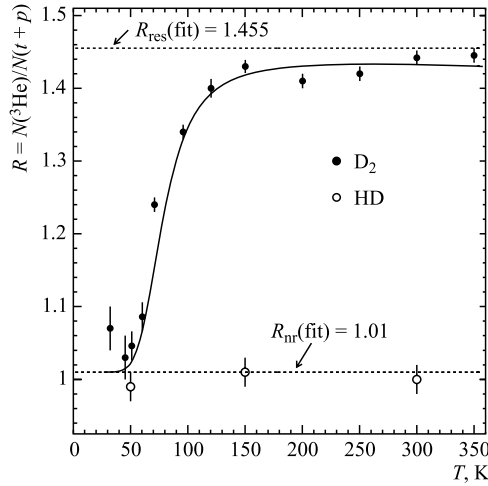
Fig. 17. Branching ratio $R = N(^3\mathrm{He} + n)/N(t + p)$ in dd fusion in D$_2$ and in HD gases plotted versus gas temperature. The solid line is the result of the fit to the D$_2$ data with Eq. (21). The dashed line is the result of the fit to the HD data with a constant value of R_{nr}

second fusion with the $t + p$ events as those events remained within the energy window 0.8–8 MeV. The trigger losses $\varepsilon_{\mathrm{tr}}$ were 0.065(7). The value of the proton smearing correction was measured to be $\varepsilon_{\mathrm{sm}} = 0.987-0.980$. All these corrections are well determined from the same experimental data set and contribute uncertainties on the level 0.8% to the measured ratio R obtained in D$_2$-94 and D$_2$-95 experiments. The results are presented in Table 7 and in Fig. 17. The three D$_2$-95 runs with exceptionally high nitrogen contamination were not used.

The procedure for extraction of the $R(T)$ values from the data of the HD experiment was different from the one described above in two points. First, the single exponential shape of the time distributions allowed one to extend the time window to smaller times, $1 \leqslant t \leqslant 7.5$ μs, thus increasing the statistics without enlarging the smearing correction. Second, the determined branching ratios were corrected for the presence of the D$_2$ admixture in the HD gas. The results are presented in Table 8 and in Fig. 17.

Table 8. $dd\mu$ **formation and spin-flip rates** (10^6 s^{-1})**, and branching ratios in HD gas**

T, K	φ, %	$\lambda_{dd\mu}^{\mathrm{HD}}$	λ_{21}	R	C_{D_2}, %	$C_{\mathrm{D}_2}^{\mathrm{chr}}$, %
300.3	4.87	0.119(6)	32.2 (fix)	1.00(2)	0.82(8)	0.78
150.3	4.78	0.080(3)	32.2 (fix)	1.01(2)	1.06(5)	1.02
50.2	4.74	0.056(8)	32.2 (1.7)	0.99(2)	1.16(3)	1.10

4.3. Analysis of Fusion Time Distributions. *4.3.1. Analysis of* D_2 *Runs.* We use the kinetics diagram presented in Fig. 1 to extract the $dd\mu$ formation rates $\Lambda_{dd\mu}^{1/2}(T)$, $\Lambda_{dd\mu}^{3/2}(T)$, and the spin flip rate $\Lambda_{21}(T)$ from the experimental time distributions of the $(^3\text{He} + {}^3\text{He}\mu)$ fusion events. The density-dependent rates in this scheme are related to the rates normalized to the liquid hydrogen density LHD

$$
\Lambda_{dd\mu}^{3/2} = \varphi\widetilde{\lambda}_{dd\mu}^{3/2}C_d, \quad \Lambda_{dd\mu}^{1/2} = \varphi\widetilde{\lambda}_{dd\mu}^{1/2}C_d, \quad \Lambda_{21} = \varphi\widetilde{\lambda}_{21}C_d,
$$
$$
\Lambda_{pd\mu} = \varphi\lambda_{pd\mu}C_p, \quad \Lambda_{dZ} = \varphi\lambda_{dZ}C_Z,
\tag{14}
$$

where $\widetilde{\lambda}_{dd\mu}^{3/2}$, $\widetilde{\lambda}_{dd\mu}^{1/2}$, $\widetilde{\lambda}_{21}$, $\lambda_{pd\mu}$, λ_{dZ} are the rates normalized to LHD, the first three of them being the *effective* rates including back-decay and nonresonant processes; φ is the density normalized to LHD; C_d and C_p are the deuterium and hydrogen atomic concentration, $C_d + C_p = 1$, and C_Z is the atomic concentration of the gas impurity.

The kinetics of Fig. 1 corresponds to a system of differential equations:

$$
\frac{dN_{3/2}}{dt} = -(\lambda_0 + \Lambda_{21} + \Lambda_{dd\mu}^{3/2} + \Lambda_{dZ} + \Lambda_{pd\mu})N_{3/2} + \Lambda_{12}N_{1/2},
$$
$$
\frac{dN_{1/2}}{dt} = -(\lambda_0 + \Lambda_{12} + \Lambda_{dd\mu}^{1/2} + \Lambda_{dZ} + \Lambda_{pd\mu})N_{1/2} + \Lambda_{21}N_{3/2}.
\tag{15}
$$

The analytical solution for the time distribution of $(^3\text{He} + {}^3\text{He}\mu)$ events according to Fig. 1 and Eq. (15) is

$$
N_{^3\text{He}}(t) = \chi_{\text{norm}}N_\mu(E_1\,e^{K_1 t} + E_2\,e^{K_2 t})\Delta t.
\tag{16}
$$

Here, $N_{^3\text{He}}(t)$ is the number of the first $(^3\text{He} + {}^3\text{He}\mu)$ fusion events detected within the time bin $\Delta t = 50$ ns used in our analysis; N_μ is the number of selected muon stops; $\chi_{\text{norm}} = (1 - \varepsilon_{\text{tr}})/(1 - \omega_d W_{\text{pileup}})$ is the normalization factor correcting for trigger losses of the $(^3\text{He} + {}^3\text{He}\mu)$ events and the difference in pile up corrections for N_μ and for $N(^3\text{He} + {}^3\text{He}\mu)$; $\varepsilon_{\text{tr}} = (6.5 \pm 0.7)\%$ in the D_2 runs. As the pile up probability of the first fusion signals with the muon signals W_{pileup} is identical to that of the second fusion signals with the first ^3He fusion signals, the difference comes from the $^3\text{He}\mu$ signals which do not have subsequent fusions. Therefore, the total pile up correction is $\omega_d W_{\text{pileup}}$, with $\omega_d = 0.12$. The value of W_{pileup}, determined directly from the time distributions, is 2–5% depending on the fusion rates, resulting in $\omega_d W_{\text{pileup}} = 0.2$–$0.6\%$.

The constants E_1, E_2, K_1, K_2 in Eq. (16) can be expressed through the rates and branching ratios entering the kinetics.

$$
K_{1,2} = -\frac{1}{2}\left[\Lambda_1 + \Lambda_2 \mp \sqrt{(\Lambda_1 - \Lambda_2)^2 + 4\Lambda_{21}\Lambda_{12}}\right],
$$
$$
E_1 = \beta_{1/2}\Lambda_{dd\mu}^{1/2}A_1 + \beta_{3/2}\Lambda_{dd\mu}^{3/2}A_3,
\tag{17}
$$
$$
E_2 = \beta_{1/2}\Lambda_{dd\mu}^{1/2}(\eta_{1/2} - A_1) + \beta_{3/2}\Lambda_{dd\mu}^{3/2}(\eta_{2/3} - A_3),
$$

where

$$\Lambda_1 = \lambda_0 + \Lambda_{dd\mu}^{1/2} + \Lambda_{12} + \Lambda_{pd\mu} + \Lambda_{dZ},$$

$$\Lambda_2 = \lambda_0 + \Lambda_{dd\mu}^{3/2} + \Lambda_{21} + \Lambda_{pd\mu} + \Lambda_{dZ},$$

$$A_1 = \frac{\Lambda_{21}}{K_1 + \Lambda_1} A_3, \tag{18}$$

$$A_3 = \frac{K_1 + \Lambda_1}{K_1 - K_2} \left[\eta_{3/2} - \frac{\eta_{1/2}}{\Lambda_{21}} (K_2 + \Lambda_1) \right].$$

The rate $\lambda_{pd\mu} = 5.6(2) \cdot 10^6$ s^{-1} [45] is known and Λ_{dZ} are determined from our experimental data (Subsec. 3.3 and Tables 2 to 5). The remaining three rates entering the above expressions $\Lambda_{dd\mu}^{3/2}$, $\Lambda_{dd\mu}^{1/2}$, Λ_{21} are to be extracted from the fits to the measured time distributions. The solution Eq. (16) consists of a transient part, dominated by the depopulation of the upper hyperfine state with the rate Λ_2, and a steady state region, where a dynamic equilibrium between the $d\mu$ spin states is reached and molecular formation proceeds with the steady state rate $\Lambda_{dd\mu} = \varphi C_d \widetilde{\lambda}_{dd\mu} = E_1$. The coefficients in Eq. (18) depend on the product $\beta_F \Lambda_{dd\mu}^F$. Our experiment provides all required information to disentangle the physically distinct quantities $\beta_F(T)$ and $\Lambda_{dd\mu}^F(T)$ in an iterative analysis procedure. First, we express β_F by the physically more meaningful quantities β_{res} and β_{nr}, the fusion branching ratios for the $dd\mu$ ($J = 1$, $v = 1$) state populated in resonant formation and the average branching ratio from states populated by nonresonant formation with rate $\lambda_{dd\mu}^{nr}(T)$, respectively,

$$\beta_F(T) = \frac{[\widetilde{\lambda}_{dd\mu}^F(T) - \lambda_{dd\mu}^{nr}(T)]\beta_{res} + \lambda_{dd\mu}^{nr}(T)\beta_{nr}}{\widetilde{\lambda}_{dd\mu}^F(T)}. \tag{19}$$

Second, the time distributions in the D_2 runs are fitted according to Eq. (16) using $\beta_{nr} = 0.500$, $\beta_{res} = 0.588$ and $\lambda_{dd\mu}^{nr} = 0.05 \cdot 10^6$ s^{-1}. This initial, already quite realistic guess for the β is obtained from Fig. 17. This fit yielded preliminary values for $\widetilde{\lambda}_{dd\mu}^F(T)$. Third, the time distributions from the HD run were analyzed (see Subsubsec. 4.3.2) to determine the $dd\mu$ formation rate $\lambda_{dd\mu}^{HD}(T)$. The preliminary rates $\widetilde{\lambda}_{dd\mu}^F(T)$ are used to correct for $dd\mu$ formation on the small residual concentration of D_2 molecules present in the HD gas. The results are presented in Table 8. The measured $\lambda_{dd\mu}^{HD}(T)$ shows a weak linear dependence with temperature:

$$\lambda_{dd\mu}^{HD}(T) = [0.257(17) \times T + 39(1)] \cdot 10^3 \text{ s}^{-1}. \tag{20}$$

For the further analysis, we assume that nonresonant formation is the same for deuterons bound in HD and D_2, $\lambda_{dd\mu}^{nr} = \lambda_{dd\mu}^{HD}(T)$.

Having determined $\lambda_{dd\mu}^{\mathrm{nr}}$, we can fit the observed $R(T)$ from the D_2 runs in the fourth step

$$R(T) = \frac{[\widetilde{\lambda}_{dd\mu}(T) - \lambda_{dd\mu}^{\mathrm{nr}}(T)]\beta_{\mathrm{res}} + \lambda_{dd\mu}^{\mathrm{nr}}(T)\beta_{\mathrm{nr}}}{[\widetilde{\lambda}_{dd\mu}(T) - \lambda_{dd\mu}^{\mathrm{nr}}(T)](1 - \beta_{\mathrm{res}}) + \lambda_{dd\mu}^{\mathrm{nr}}(T)[1 - \beta_{\mathrm{nr}}]}, \qquad (21)$$

where $\widetilde{\lambda}_{dd\mu}$ is the steady-state $dd\mu$ formation rate. Simultaneously, the data on $R(T)$ from the HD runs were fitted with the constant value

$$R_{\mathrm{nr}} = \frac{\beta_{\mathrm{nr}}}{1 - \beta_{\mathrm{nr}}}. \qquad (22)$$

From this fit shown in Fig. 17, the final values of $R_{\mathrm{res}} = 1.455(11)$ and $R_{\mathrm{nr}} = 1.01(1)$ were obtained. The corresponding branching ratios are $\beta_{\mathrm{res}} = 0.593$ and $\beta_{\mathrm{nr}} = 0.502$. With these updated values and $\lambda_{dd\mu}^{\mathrm{nr}}(T)$ from Eq. (20), the second fit to the D_2 data was performed, to determine the final rates $\widetilde{\lambda}_{dd\mu}^{F}$ and $\widetilde{\lambda}_{21}$. As their values were close to those from the first fit, no further iteration was needed. These results are presented in Table 7 and in Figs. 21 and 24. Also shown are the steady-state formation rates $\widetilde{\lambda}_{dd\mu}$ calculated from the measured $\widetilde{\lambda}_{dd\mu}^{F}$.

4.3.2. Analysis of the $(H_2 + D_2)$, HD *and* $(H_2 + 2HD + D_2)$ *Runs.* The analysis of the $(H_2 + D_2)$ experiment (nonequilibrium gas mixture) followed the procedure described above, using the atomic deuterium concentration $C_d = 0.476$ relevant for this filling. The H_2 and D_2 concentrations were determined with high precision (0.2%) by the gas pressure measurements during the gas filling, and were also controlled with a chromatograph with a precision of 2%. The results are presented in Table 6.

The analysis of the HD and $(H_2 + 2HD + D_2)$ runs required some modification of expressions (18), (19) used in the fitting procedure. In particular, the following replacements accounted for $dd\mu$ formation on both D_2 and HD molecules:

$$\Lambda_{dd\mu}^{F} \to \Lambda_{dd\mu}^{F}(D_2) + \Lambda_{dd\mu}^{F}(HD),$$
$$\beta_F \Lambda_{dd\mu}^{F} \to \beta_F(D_2)\Lambda_{dd\mu}^{F}(D_2) + \beta_F(HD)\Lambda_{dd\mu}^{F}(HD), \qquad (23)$$

with $\Lambda_{dd\mu}^{F}(D_2) = \varphi C_{D_2}\widetilde{\lambda}_{dd\mu}^{F}(D_2)$ and $\Lambda_{dd\mu}^{F}(HD) = \varphi C_{HD}\lambda_{dd\mu}^{F}(HD)/2$. $\beta_F(D_2)$ is calculated according to Eq. (19) and $\beta_F(HD) = \beta_{\mathrm{nr}}$. We assumed that the hyperfine components of the nonresonant $dd\mu$ formation rates in HD molecules are equal to each other $\Lambda_{dd\mu}^{F}(HD) = \Lambda_{dd\mu}(HD)$. Thus, the fusion time distribution in pure HD gas should be a single exponential, and observed deviation from this shape (see Fig. 14) were attributed to the D_2 admixture in the HD gas. In the fits to the HD data, the rates $\widetilde{\lambda}_{dd\mu}^{F}(D_2)$ were fixed from the D_2 data analysis, and the fitting parameters were $\lambda_{dd\mu}(HD)$, $\lambda_{21}(HD)$, and C_{D_2}. In fact, the spin flip rate $\lambda_{21}(HD)$ could be reliably determined only at $T = 50$ K: $\lambda_{21}(HD) =$

$32.2(1.7) \cdot 10^6$ s^{-1} and was fixed to this value in the fits of the 150 and 300 K data. The results are presented in Table 8 and in Fig. 21. The fitted deuterium concentrations C_{D_2} were close to the ones measured by the chromatograph — evidence for the correct interpretation of the HD data.

Table 9. $dd\mu$ **formation and spin flip rates** $(10^6$ s$^{-1})$ **in H₂/D₂ gas mixture**

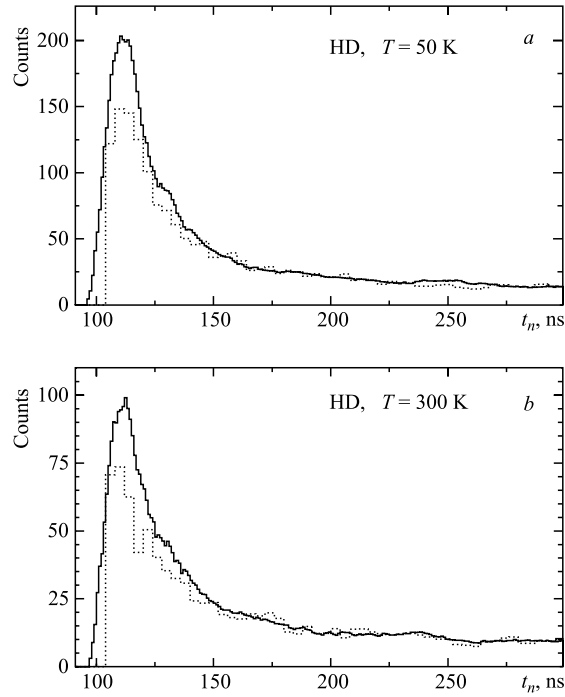| T, K	Gas	φ, %	$\widetilde{\lambda}_{dd\mu}^{1/2}$	$\widetilde{\lambda}_{dd\mu}^{3/2}$	$\widetilde{\lambda}_{dd\mu}$	$\widetilde{\lambda}_{21}$
50.2	EQ	5.07	0.058(4)	3.66(3)	0.058(4)	34.0(4)
50.2	NE	5.12	0.051(4)	3.74(3)	0.051(4)	35.5(3)
100.2	EQ	5.00	0.279(8)	4.50(5)	0.309(8)	33.9(5)
150.2	EQ	4.97	0.95(1)	4.88(5)	1.126(10)	35.6(7)
150.2	NE	5.02	0.934(10)	4.94(6)	1.11(1)	35.5(7)
300.2	EQ	4.91	2.55(6)	3.62(18)	2.80(6)	52(10)
300.2	NE	4.97	2.51(3)	3.70(7)	2.79(3)	35(5)

Fig. 18. The initial part of time distributions of neutrons from dd fusion in HD gas at $T = 50$ K (*a*) and $T = 300$ K (*b*) measured with the neutron detectors. The detected neutron rates are expressed via the $dd\mu$ formation rates normalized to LHD. The dashed histograms correspond to the Monte Carlo calculations. The prompt peak visible between 100 and 150 ns is attributed to fast molecular formation caused by epithermal muons

In the analysis of the $(H_2 + 2HD + D_2)$ runs, the rate $\Lambda_{dd\mu}(HD)$ was taken from Eq. (20). The fitting parameters, $\widetilde{\lambda}_{dd\mu}^{1/2}(D_2)$, $\widetilde{\lambda}_{dd\mu}^{3/2}(D_2)$, $\widetilde{\lambda}_{21}$ are presented in Table 9. Measurements of time distributions of fusion neutrons in the HD experiment revealed a prominent peak at $T_N = (t_n - t_n^0) < 50$ ns (Fig. 18). It is interpreted as contribution of $dd\mu$ formation in HD molecules by the epithermal $d\mu$ atoms with kinetic energies higher than 0.3 eV (see Subsec. 5.3).

5. DISCUSSION

5.1. Muon Sticking. Soon after the discovery of muon catalyzed fusion, Jackson [46] recognized the importance of muon sticking as a fundamental limitation for the number of fusion cycles catalyzed per muon. He calculated muon stripping while the $He\mu$ atom is slowing down, and concluded that this reactivation process does not decrease appreciably the muon loss by sticking, with the results $\omega_d^0 = 16\%$ and $\mathcal{R} = 0.04-0.13$ [46]. A calculation by Gershtein et al. [47] in 1981 yielded $\omega_d^0 = 15.5\%$, $\mathcal{R} = 0.05$, $\omega_d = 14.7\%$.

The first experimental result $\omega_d = (12.2 \pm 0.3)\%$ by the Gatchina group [18] in 1983, proved to be slightly below the theoretical prediction [47]. This disagreement became even larger when calculations extended the approach used in [47], which included excited $^3He\mu$ states up to $n = 3$, to higher n states, which increased ω_d^0 to 17.2% [48]. The problem proved to be in the calculation of the $dd\mu$ wave function $\psi_{dd\mu}(r, \rho)$ at small inter-nuclear distances $\rho \to 0$. References [46, 47] had calculated it in the Born–Oppenheimer approximation assuming that the muon follows the motion of the nuclei adiabatically. Further work focused on finding the united-nuclei limit of the correct nonadiabatic wave functions of the muonic molecules using the adiabatic representation [48] and variational methods [49, 50]. The calculated values of the initial sticking probability were close to each other (Table 10). We average those to obtain the best theoretical prediction $\omega_d^0 = 13.7\%$.

The calculation of the final sticking probability ω_d requires knowledge of the muon reactivation processes. According to theory, 30% of the $^3He\mu$ atoms are produced in excited states. While the muonic atom ionization cross section is higher in excited states, ionization competes with very fast radiative de-excitation. Therefore, excited states contribute to muon stripping only at high gas densities, while at low gas densities the stripping occurs mostly from the ground state with additional contribution from the $2s$ metastable state of the $^3He\mu$ atom. A comprehensive calculation of the muon reactivation process requires a kinetics treatment that takes into account collisional excitations and de-excitations, ionization, muon transfer, and radiation. The rates of these processes are known mainly from theoretical calculations. In Table 10, the predicted dependence of the muon reactivation coefficient on the gas density φ is shown. At our experimental conditions, the increase $\Delta\varphi = +0.04$ should increase $\mathcal{R}$ by $\Delta\mathcal{R} = +0.01$. Within

Table 10. **Theoretical calculations of muon sticking and reactivation probabilities in** $dd\mu$ **fusion**

Authors and Refs.	Year	ω_d^0, %	$\mathcal{R}(\varphi = 1.2)$	$\mathcal{R}(\varphi)$
Jackson [46]	1957	16	0.04–0.13	
Gershtein et al. [47]	1981	15.5	0.05	
Bogdanova et al. [48]	1985	13.7*		
Hu, Kaufmann [49]	1987	13.08		
Haywood et al. [50]	1991	13.40		
Abramov et al. [54]	1996	13.98		
Frolov [55]	2001	14.04		
Men'shikov and Ponomarev [56]	1985		0.17	0.07 ($\varphi = 0.07$)
Struensee, Cohen [51]	1988		0.18	0.104 ($\varphi = 0.07$)
Markushin [52]	1988		0.17	0.10 ($\varphi = 0.1$)
Takahashi [53]	1988		0.14	0.11 ($\varphi = 0.1$)

*After correction in [52]. Original result was 13.3%.

the experimental uncertainty our data agree with this prediction:

$$\Delta\mathcal{R}^{\mathrm{exp}} = \frac{\omega_d(\varphi = 0.0485) - \omega_d(\varphi = 0.0837)}{\omega_d^0} = 0.008(8).$$

Taking into account the theoretical φ dependence of the muon reactivation and averaging the results from the latest analyses [51–53], we obtain $\mathcal{R}^{\mathrm{th}}(\varphi = 0.07) = 0.10 \pm 0.01$ and $\omega_d^{\mathrm{th}}(\varphi = 0.07) = (\omega_d^0)_{\mathrm{th}}(1 - \mathcal{R}^{\mathrm{th}}) = 0.123(4)$. Within the quoted error, this result agrees with our experimental results given in Eq. (11). This can be considered as evidence for the overall consistency and correctness of the modern theory on initial muon sticking and muon reactivation in muon catalyzed dd fusion. Note, however, that, as concerns $\mathcal{R}$, our experiment corresponds to relatively low gas densities where the muon stripping is dominated by the ionization collisions of the ground-state ^{3}Heμ atoms.

5.2. Charge Asymmetry in $dd\mu$ **Fusion.** The large asymmetry in the yields of the mirror reactions $dd \to {}^3\mathrm{He} + n$ and $dd \to t + p$ in $dd\mu$ fusion, first observed in the Gatchina experiment in 1983 [18], remained unexplained for several years. It was understood only that it occurs in the P-wave dd interaction, while the fusion remains nearly symmetric in the S-wave.

A similar asymmetry in the P-wave dd interaction was observed earlier in a low energy dd scattering experiment [57]. Unlike the scattering experiment, where the P-wave constitutes only a small fraction of the total scattering amplitude, in the $dd\mu$ molecules formed in the $J = 1$ state, the two deuterons are prepared in pure $L = 1$ state of relative angular momentum, and fusion takes place at virtually zero energy [58]. On the other hand, the dd fusion from the $J = 0$

$dd\mu$ states occurs in the $L = 0$ state. This picture was implemented in the analysis presented above which allowed to determine the branching ratio $R_{\text{res}} = Y(^3\text{He} + n)/Y(t + p)$ for dd fusion from the $J = 1$, $v = 1$ $dd\mu$ state: $R_{\text{res}} = R_{J=1} = 1.455(11)$. This can be compared with the dd scattering experiment [57] where the branching ratio was measured both in the P-wave and in the S-wave: $R_{L=1} = 1.459(16)$ and $R_{L=0} = 0.902(5)$. The agreement between the results of these quite different experiments confirms the validity of the mechanism of dd fusion in the $dd\mu$ molecule.

An explanation of the origin of the charge asymmetry in the $dd\mu$ fusion was suggested by Hale in 1990 [59]. His calculations using a charge-independent R-matrix description of reactions in the $A = 4$ system yielded $R_{L=1} = 1.43$ and $R_{L=0} = 0.886$. The large deviation of $R_{L=1}$ from unity is attributed to the small effects of internal Coulomb isospin mixing being greatly amplified in the external Coulomb field by the proximity of broad levels having opposite isospin in the P-wave states.

5.3. Nonresonant Formation of $dd\mu$ Molecules. The theory of nonresonant formation of muonic molecules based on the Auger process shown in Eq. (1) was formulated even before the experimental discovery of μCF and was gradually developed to accurately calculate $dd\mu$ formation into the states presented in Table 11. Molecular formation proceeds from various initial orbital momentum J_i states in the $d\mu + d$ system to various J, v states of the final $dd\mu$ molecule. At low temperature the initial state is mostly $J_i = 0$, and the dominating rates are $\lambda^{\text{nr}}_{J=1} = 0.012 \cdot 10^6$ s^{-1} ($E1$ transition from $J_i = 0$ to $J = 1$, $v = 0$) and $\lambda^{\text{nr}}_{J=0} = 0.015 \cdot 10^6$ s^{-1} ($E0$ transition from $J_i = 0$ to $J = 0$, $v = 1$). With increasing temperature, $\lambda^{\text{nr}}_{J=0}$ increases due to the $E1$ transition from $J_i = 1$ to $J = 0$, $v = 1$. Theory predicts a linear dependence of $\lambda^{\text{nr}}_{J=0}$ with temperature at $T < 10^3$ K [60]:

$$\lambda^{\text{nr}}_{J=0} = (0.24 \times T + 15) \cdot 10^3 \text{ s}^{-1}. \tag{24}$$

On the other hand, no significant dependence on temperature is expected for $\lambda^{\text{nr}}_{J=1}$.

Table 11. **Calculated nonresonant $dd\mu$ formation rates at the CMS energy 0.04 eV in the $d\mu + d$ system [60]**

Initial state (J_i)	$dd\mu$ state (J, v)	$\lambda^{\text{nr}}_{dd\mu}$ (10^6 s^{-1})
0	(0,0)	$0.227 \cdot 10^{-4}$
1	(0,0)	$0.212 \cdot 10^{-4}$
0	(1,0)	$0.118 \cdot 10^{-1}$
1	(1,0)	$0.983 \cdot 10^{-5}$
2	(1,0)	$0.348 \cdot 10^{-7}$
1	(2,0)	$0.274 \cdot 10^{-2}$
0	(0,1)	$0.150 \cdot 10^{-1}$
1	(0,1)	$0.740 \cdot 10^{-1}$

In the HD experiment, the total $dd\mu$ formation rate at temperatures from 50 to 300 K as given in Eq. (20) was measured. According to the theory, the $dd\mu$ formation on HD molecules should be purely nonresonant in this temperature region and resonance condition could be reached only at very high temperatures ($T > 10^3$ K). Therefore, the observed $\lambda_{dd\mu}$(HD) is expected to be the nonresonant $dd\mu$ formation rate $\lambda_{dd\mu}^{\mathrm{nr}}$. This rate has two components

$$\lambda_{dd\mu}^{\mathrm{nr}}(T) = \lambda_{J=0}^{\mathrm{nr}}(T) + \lambda_{J=1}^{\mathrm{nr}}(T). \tag{25}$$

Noting that the transitions to $J = 1$ and to $J = 0$ $dd\mu$ states lead to significantly different branching ratios $\beta_{J=1}$ and $\beta_{J=0}$, we can determine the ratio of these two components using β_{nr} measured in the HD experiment

$$\frac{\lambda_{J=0}^{\mathrm{nr}}}{\lambda_{J=1}^{\mathrm{nr}}} = \frac{\beta_{\mathrm{nr}} - \beta_{J=1}}{\beta_{J=0} - \beta_{\mathrm{nr}}}. \tag{26}$$

The HD data (Fig. 17) are consistent with $R_{\mathrm{nr}} = 1.01$ ($\beta_{\mathrm{nr}} = 0.502$), constant in the measured temperature range. Using the $\beta_{J=1} = 0.593$ from this experiment and $\beta_{J=0} = 0.474$ from the dd scattering experiment [57], we obtain $\lambda_{J=0}^{\mathrm{nr}}/\lambda_{J=1}^{\mathrm{nr}} = 3.2$, valid for the measured temperature range $50 \leqslant T \leqslant 300$ K. This implies that not only $\lambda_{J=0}^{\mathrm{nr}}$ but also $\lambda_{J=1}^{\mathrm{nr}}$ depend on temperature. More explicitly, this dependence was obtained from a fit to the experimental points shown in Fig. 17 with fixed $\beta_{J=0} = 0.474$, with $\lambda_{dd\mu}^{\mathrm{nr}}(T)$ given by Eq. (25), and with a function $\lambda_{J=1}^{\mathrm{nr}}(T)$ linearly-dependent on temperature. The result is

$$\lambda_{J=1}^{\mathrm{nr}}(T) = (0.054(24) \times T + 10(2)) \cdot 10^3 \ \mathrm{s}^{-1} \tag{27}$$

with the uncertainties arising from the errors in $R(T)$ and $\lambda_{dd\mu}^{\mathrm{nr}}(T)$. Figure 19 indicates that theory well describes nonresonant formation by the $E1$ transitions $\lambda_{J=1}^{\mathrm{nr}}$ ($T \rightarrow 0$) and the temperature dependence of $\lambda_{J=0}^{\mathrm{nr}}(T)$. On the other hand, the calculated rate of the $E0$ transition, $\lambda_{J=0}^{\mathrm{nr}}$ ($T \rightarrow 0$), appeared to be a factor of 2 lower than the experimental value. Also, the observed very weak temperature dependence of $\lambda_{J=1}^{\mathrm{nr}}(T)$ requires some explanation.

According to the theory, $\lambda_{dd\mu}^{\mathrm{nr}}$ continues to rise with $d\mu$ kinetic energy reaching a maximum value of $4 \cdot 10^6$ s^{-1} around $E_{d\mu} = 7$ eV. Then it is decreasing slowly down to $1 \cdot 10^6$ s^{-1} at $E_{d\mu} = 50$ eV [60]. Moreover, there should be a significant increase of $\lambda_{dd\mu}^{\mathrm{HD}}$ at $E_{d\mu} = 0.3-0.4$ eV due to resonant $dd\mu$ formation in the HD molecules as shown in Fig. 20. Thus $\lambda_{dd\mu}^{\mathrm{HD}}$ for epithermal $d\mu$ atoms with $E_{d\mu} > 1$ eV is expected to be more than ten times higher than at $T = 50-300$ K. Such behavior explains the observed sharp peak in the initial part of the neutron time distributions in the HD-experiment (Fig. 18). Indeed, we can expect that, even in pure D_2 gas, the kinetic energy of a major part of the $d\mu$ atoms exceeds 1 eV after the de-excitation cascade. This expectation is
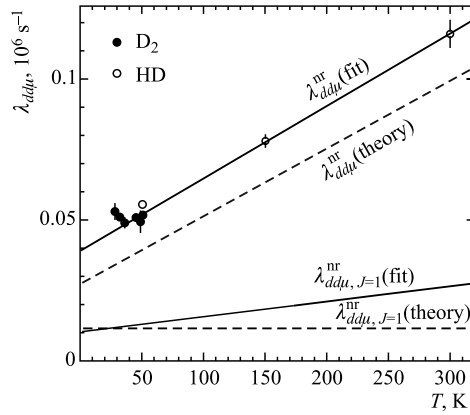
Fig. 19. Nonresonant $dd\mu$ formation rates on HD and D_2 molecules versus temperature. The dashed lines correspond to the theory. The solid lines represent the best fit to experimental data
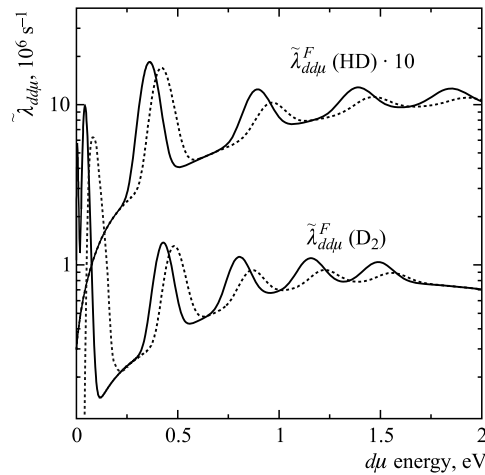

Fig. 20. Calculated $dd\mu$ formation rates in HD and D_2 gases versus energy of the $d\mu$ atom [60,61]. Solid and dashed curves correspond to the total spin of the $d\mu$ atom $F = 3/2$ and $F = 1/2$, respectively

based on experimental studies of the kinetic energy of $\pi^- p$ atoms in hydrogen gas at 40 bar pressure [24], and is supported from measured muonic cascade yields [25,26,29] and corresponding simulations [62].

In HD gas, the high-energy component should be enhanced due to the muon transfer Eq. (4). At our experimental conditions, muon transfer from the ground

state of the $p\mu$ atom is expected with $\sim 50\%$ probability [62], with the $d\mu$ atoms receiving a kinetic energy of 43 eV, while excited pμ state transfer leads to $d\mu$ kinetic energies exceeding 0.3 eV. The shapes of the peaks in Fig. 18 are determined by the thermalization of the $d\mu$ atoms passing through the region of high $dd\mu$ formation rates at epithermal energies. The formation rate drops to twice the thermalized rate at 50 K within 60 ns after the muon stop. This corresponds approximately to the $d\mu$ atom mean kinetic energy of 0.04 eV. The full thermalization requires about 250 ns. The measured neutron distributions (Fig. 18) were reproduced with a Monte Carlo simulation with a programme code from [63] using the theoretical $p\mu$ and $d\mu$ scattering cross sections [64] and the $dd\mu$ formation rates [60,61]. The energy distribution of the $p\mu$ and $d\mu$ atoms after the cascade was taken from [62]. The results are in qualitative agreement with the data. In pure D_2 the epithermal and thermal formation rates are comparable to each other and the thermalization rate of $d\mu$ atoms is a factor of two higher than in HD. No visible epithermal peaks in the time distributions were observed in this case.

5.4. Spin Flip Rates in $d\mu$ Atoms. Tables 7–9 present the spin flip rates $\widetilde{\lambda}_{21}$ measured in pure D_2 and in the H_2/D_2 gas mixtures. Figure 21 shows these rates together with results from the previous experiments [16]. The new results have higher precision and cover a larger temperature range, and otherwise agree well with the previous data. A comparison of the spin flip rates in pure D_2 and in $H_2 + D_2$ nonequilibrium gas mixture done at $T = 50$ K and $T = 150$ K
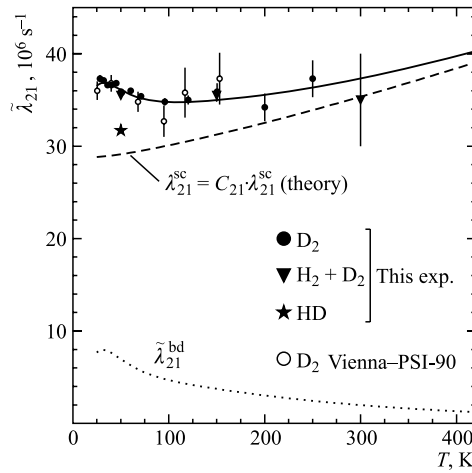

Fig. 21. Spin-flip rates in $d\mu$ atoms measured in D_2 and HD gases. Also the theoretical distributions $\widetilde{\lambda}_{21}(T)$ (solid line), $\lambda_{21}^{\mathrm{sc}}(T)$ and $\widetilde{\lambda}_{21}^{\mathrm{bd}}(T)$ are presented, following from simultaneous fitting to the experimental data on $\widetilde{\lambda}_{21}(T)$ and $\widetilde{\lambda}_{dd\mu}^{F}(T)$ as explained in Subsec. 5.5 (fit C in Table 13). The normalization parameter found from the fit is $C_{21} = 0.59(1)$

shows that the hyperfine transition rate from collisions of $d\mu$ atoms with the H_2 molecules is negligible,

$$\lambda_{21}(H_2) = \widetilde{\lambda}_{21}(H_2 + D_2) - \widetilde{\lambda}_{21}(D_2) \leqslant 0.3 \cdot 10^6 \text{ s}^{-1}.$$

Note that the lower C_d concentration in the $H_2 + D_2$ experiment allowed to measure $\widetilde{\lambda}_{21}$ up to $T = 300$ K.

The spin flip in D_2 gas may occur either in inelastic nonresonant scattering of the $d\mu$ atoms on the D_2 molecules or via back-decay of the resonantly formed $dd\mu$ molecule: $\widetilde{\lambda}_{21}(D_2) = \lambda_{21}^{sc}(D_2) + \widetilde{\lambda}_{21}^{bd}$. On the other hand, the spin flip rate in the HD gas contains only the nonresonant scattering component. In our HD experiment, $\lambda_{21}(HD)$ was determined at $T = 50$ K in two different ways. First, the spin flip rate was obtained from the slope of the fusion time distribution (due to the presence of a small D_2 admixture in the HD gas). The result $\lambda_{21}(HD) = 32.2(1.7)$ is presented in Table 8. In the second method, $\lambda_{21}(HD)$ was extracted from the value of $\widetilde{\lambda}_{21}$ measured in the $H_2 + 2HD + D_2$ experiment at $T = 50$ K using the known value of $\widetilde{\lambda}_{21}(D_2)$ and also C_{D_2} and C_{HD} concentrations shown in Table 6. The result $\lambda_{21}(HD) = 31.7(7)$ is shown in Fig. 21. The spin flip rate in the HD gas at $T = 50$ K is noticeably lower than in the D_2 gas. In principle, this difference might be used to determine the back-decay rate $\widetilde{\lambda}_{21}^{bd} = \widetilde{\lambda}_{21}(D_2) - \lambda_{21}(HD)$. However, before using this equation, one should correct it for differences in the hyperfine transition rates $\lambda_{21}^{sc}(HD)$ and $\lambda_{21}^{sc}(D_2)$ in inelastic scattering on deuterons bound in HD or D_2 molecules, respectively. Theoretical calculations [65] predict a $\sim 8\%$ higher rate $\lambda_{21}^{sc}(HD)$ at $T = 50$ K than $\lambda_{21}^{sc}(D_2)$.

Unfortunately, there exists a long-standing unresolved discrepancy between theory and experiment [16] concerning the spin flip rates in D_2 gas. The problem is that the theoretical spin flip rate via nonresonant scattering of the $d\mu$ atoms on the D_2 molecules, $\lambda_{21}^{sc}(T)$, considerably exceeds the measured total spin flip rate $\widetilde{\lambda}_{21}(T)$ even without subtraction from this value of the back-decay rate $\widetilde{\lambda}_{21}^{bd}(T)$. Therefore, assuming the theoretical problems are related with the absolute scale, the theoretical functions [65] multiplied by a free normalization factor C_{21} were used in the fit. This procedure is described in the next Section. The quality of the fit (Fit C, Table 13) is demonstrated in Fig. 21. Note that this analysis allowed one to determine both $\lambda_{21}^{sc}(T) = C_{21}\lambda_{21}^{sc}(\text{theory})$ and $\widetilde{\lambda}_{21}^{bd}(T)$ as shown in Fig. 21. Our analysis indicates relatively small contribution to the spin flip rate from the back-decay of the $dd\mu$ molecule, the dominating contribution being due to λ_{21}^{sc}. However, the size of λ_{21}^{sc} proved to be much lower than $\lambda_{21}^{sc}(\text{theory})$ with renormalization factor $C_{21} = 0.59(1)$, confirming the normalization factor ≈ 0.6 observed in Vienna–PSI experiment [17]. Note that the value of $\lambda_{21}^{sc}(D_2)$ obtained this way at $T = 50$ K is lower than $\lambda_{21}^{sc}(HD)$ by $\sim 7\%$ in agreement with the theoretical calculations mentioned above.

5.5. Resonant Formation of $dd\mu$ **Molecules.** The progress in μCF theory achieved in the last decades allows one to calculate the resonant $dd\mu$ formation rates *ab initio*, i.e., without introducing any free parameter. In the following, a detailed comparison between this theory and experiment was performed by fitting our data with the theoretical expressions. The approach follows the scheme of theoretical analysis of the Vienna–PSI experiment in 1993 [17], but is more comprehensive due to further refinements in the theoretical calculations and due to the higher precision data set covering a wider temperature range from 28 to 350 K.

The *effective* $dd\mu$ formation rates $\widetilde{\lambda}_{dd\mu}^{F}$ and the hyperfine transition rate $\widetilde{\lambda}_{FF'}$ are expressed as the sum of nonresonant and resonant terms [37]:

$$\widetilde{\lambda}_{dd\mu}^{F} = \lambda_{dd\mu}^{\mathrm{nr}} + \sum_{S} \frac{\lambda_{FS}\widetilde{\lambda}_f}{\widetilde{\lambda}_f + \Gamma_S}, \tag{28}$$

$$\widetilde{\lambda}_{FF'} = \lambda_{FF'}^{\mathrm{sc}} + \sum_{S} \frac{\lambda_{FS}\Gamma_{SF'}}{\widetilde{\lambda}_f + \Gamma_S}. \tag{29}$$

The nonresonant $dd\mu$ formation rate $\lambda_{dd\mu}^{\mathrm{nr}}(T)$ was calculated according to Eq. (20), the spin flip rate $\lambda_{FF'}^{\mathrm{sc}}(T)$ was taken from [65]. The effective fusion rate $\widetilde{\lambda}_f$ is the sum of the dd fusion and de-excitation rates of the $(J = 1, v = 1)$ state of $dd\mu$ formed in resonant formation [37].
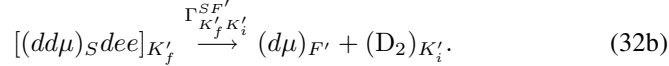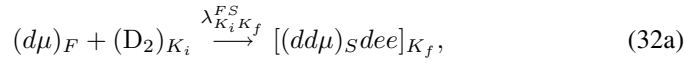
The rates of resonant formation λ_{FS}

$$\lambda_{FS} = \sum_{K_i, K_f} \omega_i(K_i)\lambda_{K_iK_f}^{FS} \tag{30}$$

and back-decay Γ_{SF}

$$\Gamma_{SF} = \sum_{K_iK_f} \omega_f(K_f)\Gamma_{K_fK_i}^{SF}, \quad \Gamma_S = \sum_{F}\Gamma_{SF} \tag{31}$$

are weighted sums over individual transitions in reactions

$$(d\mu)_F + (\mathrm{D}_2)_{K_i} \xrightarrow{\lambda_{K_iK_f}^{FS}} [(dd\mu)_S dee]_{K_f}, \tag{32a}$$

$$[(dd\mu)_S dee]_{K'_f} \xrightarrow{\Gamma_{K'_fK'_i}^{SF'}} (d\mu)_{F'} + (\mathrm{D}_2)_{K'_i}. \tag{32b}$$

Here F is the total spin of the $d\mu$ atom; the D$_2$ molecule is in the rotational state K_i; S is the total spin of the $dd\mu$ muonic molecule which is the «heavy nucleus» of the complex MD (M$^+ \equiv [dd\mu]^+$) formed in the rotational state K_f. The indices of vibrational states of the molecular systems have been omitted, since

only the transitions from initial $\nu_i = 0$ of D_2 to the final $\nu_f = 7$ of MD state contribute to the resonant formation rates at the present experiment conditions.

The formation rates $\lambda_{K_i K_f}^{FS}$ were calculated assuming an infinitely narrow width of the resonances [35–37, 66]. Another scheme of calculating the resonant formation rates was presented in [67]. Leaving aside the discussion of differences between these two calculation schemes which is beyond the framework of the present paper, note that the results of both calculations are in qualitative agreement with each other.

Both $\lambda_{K_i K_f}^{FS}$ and $\Gamma_{K_f K_i}^{SF}$ are proportional to the transition matrix elements $|V_{if}|^2$ with explicit expressions given in [37, 61]:

$$\lambda_{K_i K_f}^{FS} = 2\pi N_0 \frac{(2S+1)W_{SF}f(\varepsilon_{\rm res}, T)}{(2F+1)(2S_d+1)}|V_{if}(\epsilon_{\rm res})|^2, \tag{33a}$$

$$\Gamma_{K_f K_i}^{SF} = \frac{(\mu^3 \varepsilon_{\rm res})^{1/2}}{\pi} \frac{(2K_i+1)W_{SF}}{(2K_f+1)(2J+1)}|V_{if}(\epsilon_{\rm res})|^2. \tag{33b}$$

Here N_0 is the atomic number density in LHD; $f(\varepsilon, T)$ is the Maxwellian distribution of the $d\mu + D_2$ over collision energies ε; the factor W_{SF} accounts for the overlap of the initial and final spin functions.

The function $\omega_i(K_i)$ in Eq. (30) refers to the Boltzmann distribution of D_2 rotational states

$$\omega_i(K_i) = \xi(K_i)\frac{2K_i+1}{Z_i}\exp\left(-\frac{\varepsilon(K_i)}{kT}\right), \quad \sum_{K_i}\omega_i(K_i) = 1, \tag{34}$$

describing the specific experimental situation. At our experiments, the ratio of the D_2 molecules in even and odd (ortho- and para-) rotational states was equal to 2.4, and this ratio was conserved in all runs. Therefore, the terms in Eq. (34) related to even and odd states have to be normalized separately by factors

$$Z_i = \sum_{K_i}(2K_i+1)\exp\left(-\frac{\varepsilon(K_i)}{kT}\right), \quad K_i = \text{even or odd}$$

with the corresponding weights

$$\xi(K_i) = \begin{cases} \dfrac{2.4}{3.4} & \text{for } K_i = \text{even}, \\[2mm] \dfrac{1}{3.4} & \text{for } K_i = \text{odd}. \end{cases} \tag{35}$$

The validity of calculating Γ_{SF} by the expression Eq. (31) where the function $\omega_f(K_f)$ describes the distribution of the MD complex over rotational energies was discussed in [17, 37]. There it was pointed out that the proper averaging

procedure over rotational states depends on the target density. In the present work thermalization of rotational states before back-decay or fusion was assumed, leading to a Boltzmann distribution in $\omega_f(K_f)$.

The transition matrix elements $|V_{if}|^2$ were calculated according to the model of resonant formation of muonic molecules developed in [37,66] with the interaction operator $\hat{V}$ expanded up to quadrupole terms [61]. The wave functions of the initial and final states of molecular systems were derived in [68], and the normalization constant of the $dd\mu$ molecule wave function was taken as $C = 0.678$ [66].

Energy conservation in Eq. (32a) requires that the relative energy of the $d\mu$+D$_2$ collision plus the energy of the inital bound states equals the energy of the excited final state. Thus the collision energy must equal $\varepsilon_{\rm res}$ as defined by the following conditions:

$$\varepsilon_{\rm res} = \Delta E_{FS} + \Delta E_{K_i K_f}, \tag{36}$$

$$\Delta E_{FS} = \varepsilon_{11} + \delta\varepsilon_{dd\mu}(S) - \delta\varepsilon_{d\mu}(F), \tag{37}$$

$$\Delta E_{K_i K_f} = E_{70}^{\rm MD} + E_{00}^{\rm MD} - E_{00}^{\rm D_2} + \Delta E_{if}, \tag{38}$$

$$\Delta E_{if} = \varepsilon(K_f) - \varepsilon(K_i), \tag{39}$$

$$\Delta\varepsilon_{d\mu}^{F} = \delta\varepsilon_{d\mu}(F = 3/2) - \delta\varepsilon_{d\mu}(F = 1/2), \tag{40}$$

$$\Delta\varepsilon_{dd\mu}^{S} = \delta\varepsilon_{dd\mu}(S = 3/2) - \delta\varepsilon_{dd\mu}(S = 1/2), \tag{41}$$

where ε_{11} is the energy of the $dd\mu$ molecule loosely bound state ($\varepsilon_{11} = -|\varepsilon_{Jv}|$) with the angular momentum $J = 1$ and the vibrational quantum number $v = 1$; $\delta\varepsilon_{dd\mu}(S)$ and $\delta\varepsilon_{d\mu}(F)$ are the hyperfine shifts of the energy levels in $dd\mu$ and $d\mu$, respectively, as shown in Fig. 22; $E_{00}^{\rm MD}$ and $E_{00}^{\rm D_2}$ are the ground-state energies of the muonic complex ($\nu = 0, K_f = 0$) and the D$_2$ molecule ($\nu = 0, K_i = 0$), respectively; $\varepsilon(K_f)$ and $\varepsilon(K_i)$ stand for rotational energies relative to the corresponding vibrational levels of the muonic complex ($E_{70}^{\rm MD}$) and the D$_2$ molecule ($E_{00}^{\rm D_2}$). Those have been calculated in [69].
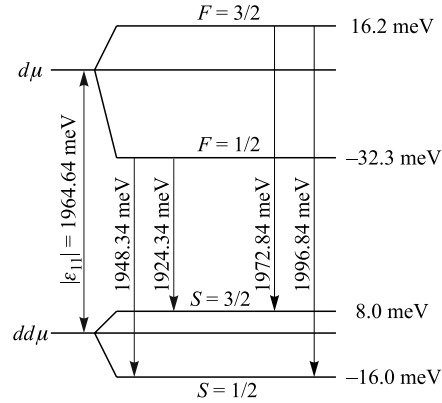

Fig. 22. Scheme of hyperfine structure of energy levels in the muonic $d\mu$ atoms and $dd\mu$ molecules. $F = S_\mu + S_d$ — total spin of $d\mu$ atoms, $S = S_\mu + S_d + S_d$ — total spin of $dd\mu$ molecule. The numbers on the right side of the figure are hyperfine shifts $\delta\varepsilon_{d\mu}(F)$ and $\delta\varepsilon_{dd\mu}(S)$

The hyperfine structure[1] of the $d\mu$ atom ground and of the $dd\mu$ molecule ($J = v = 1$) states was calculated in [38] with cited precision better than 0.1 meV. This structure as well as the energies ΔE_{FS} of $F \to S$ transitions are shown in Fig. 22.

The value $\varepsilon_{11} = -1.96464$ eV calculated as the sum of the nonrelativistic energy $\varepsilon_{11}^{\mathrm{nr}}$ of the ($J = v = 1$) state of the $dd\mu$ molecule [34] and several corrections is presented in Table 12. These corrections are estimated to be accurate to ~ 0.1 meV [70], except the finite-size correction which has an uncertainty of ≈ 0.4 meV, estimated from the difference between the results of calculation [70] and [71]. The first calculation of the correction to ε_{11} was done in [72].

Table 12. **Corrections to the nonrelativistic energy $\varepsilon_{11}^{\mathrm{nr}}$ of the ($J = 1$, $v = 1$) $dd\mu$ molecule in meV**

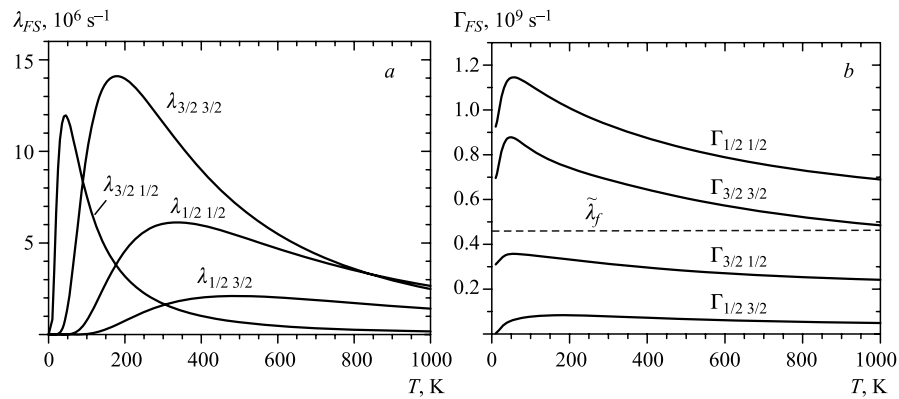|		
Vacuum polarization	8.62	[70]
Electromagnetic structure of nuclei	−1.67	[70]
Relativistic	1.65	[70]
Finite-size correction	1.85	[71]
Nuclear polarization	−0.1	[70]
Total shift	**10.35**	
Nonrelativistic energy $\varepsilon_{11}^{\mathrm{nr}}$	−1974.985	[34]
Total energy ε_{11}	**−1964.64**	

Fig. 23. Calculated $dd\mu$ formation and back-decay rates: *a*) temperature dependence of hyperfine components of $dd\mu$ formation rates; *b*) temperature dependence of hyperfine components of $dd\mu$ back-decay rate. Also is shown the effective fusion rate $\widetilde{\lambda}_f$ in the ($J = 1$, $v = 1$) state of the $dd\mu$ molecule

---

[1]The smaller energy splitting (e.g., fine structure [38]) is negligible for the present analysis.

The rates λ^{FS} and Γ_{SF} were calculated according to Eq. (30)–(31), with results shown in Fig. 23. The lowest resonance is due to the $(F = 3/2, \nu_i = 0, K_i = 0)$ to $(S = 1/2, \nu_f = 7, K_f = 1)$ transition with $\Delta E_{FS} = -1996.8$ meV and $\Delta E_{K_i K_f} = 2002.2$ meV. This resonance occurs at $T \approx 50$ K ($\varepsilon_{\mathrm{res}} = 5.4$ meV) and leads to the dominance of $\lambda_{3/2\ 1/2}$ at low temperatures.

The dashed curves in Fig. 24 show $\widetilde{\lambda}_{dd\mu}^{F}(T)$ calculated without any free parameter in comparison with our experimental data. The observed behavior of $\widetilde{\lambda}_{dd\mu}^{F}(T)$ is qualitatively reproduced by the theory, except the temperature region $T \leqslant 50$ K where the theory predicts significantly lower values of $\widetilde{\lambda}_{dd\mu}^{3/2}(T)$. In the following we tried to improve the agreement with the experiment by varying some parameters of the theory to fit the precise experimental data. Either the direct physics parameters

$$\epsilon_{11} \text{ — the energy of } dd\mu \text{ molecule};$$

$$\widetilde{\lambda}_f \text{ — the effective } dd\text{-fusion rate},$$

or scaling factors for theoretical parameters were chosen as fit variables. The latter were introduced by the following substitutions:

$$
\begin{aligned}
&C_{21} \text{ in Eq. (29)}: &&\lambda_{21}^{\mathrm{sc}} \to C_{21}\lambda_{21}^{\mathrm{sc}}; \\
&C_m \text{ in Eq. (33)}: &&|V_{if}| \to C_m|V_{if}|; \\
&C_{\mathrm{MD}} \text{ in Eq. (39)}: &&\varepsilon(K_f) \to C_{\mathrm{MD}}\varepsilon(K_f); \\
&C_F \text{ in Eq. (40)}: &&\Delta\varepsilon_{d\mu}^{F} \to C_F\Delta\varepsilon_{d\mu}^{F}; \\
&C_S \text{ in Eq. (41)}: &&\Delta\varepsilon_{dd\mu}^{S} \to C_S\Delta\varepsilon_{dd\mu}^{S}.
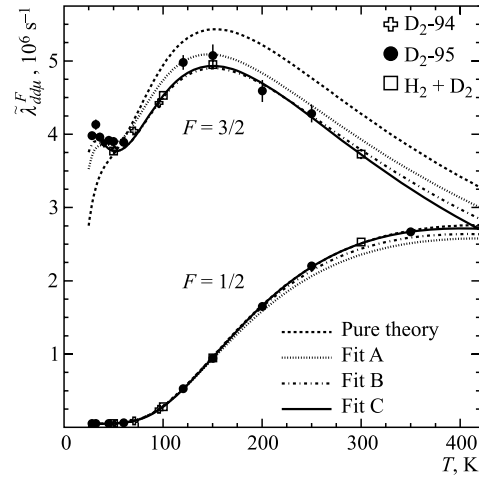\end{aligned}
$$

Fig. 24. The effective $dd\mu$ formation rates versus temperature measured in D$_2$ and H$_2$ + D$_2$ gas mixtures. The dashed curves correspond to an *ab initio* calculation, the solid curves are the best theory fit with some adjustable parameters

Table 13. **Theoretical parameters extracted from the fit to the measured rates** $\widetilde{\lambda}^{3/2}_{dd\mu}(T)$, $\widetilde{\lambda}^{1/2}_{dd\mu}(T)$, $\widetilde{\lambda}_{21}(T)$

Parameter	Theory	Fit A (O/P = 2.4/1, 28–350 K)	Fit B (O/P = 2.4/1, 28–350 K)	Fit C (O/P = 2.4/1, 28–350 K)	Fit D (O/P = 2.4/1, 28–150 K)	Fit E (O/P = 2.0/1.0, 28–350 K)	Fit F (Ortho = 100%, 28–350 K)
ε_{11}, eV	-1.9646	-1.96558(4)	-1.96511(4)	-1.96460(23)	-1.96542(36)	-1.96458(23)	-1.96484(23)
$\widetilde{\lambda}_f$, 10^6 s^{-1}	460	381(5)	375(7)	388(12)	378(14)	394(13)	347(9)
C_m	1	1.06(2)	0.90(2)	0.83(2)	0.79(3)	0.82(2)	0.85(2)
C_{21}	1	0.50(1)	0.56(1)	0.59(1)	0.60(1)	0.59(1)	0.59(1)
C_F	1	—	—	1.018(3)	1.010(4)	1.019(3)	1.010(3)
C_S	1	—	—	0.990(11)	0.960(16)	0.992(11)	0.977(11)
C_{MD}	1	—	0.834(5)	0.73(2)	0.74(2)	0.74(2)	0.69(2)
χ^2	—	310/(45-4)	112/(45-5)	47.5/(45-7)	35.4/(35-7)	47.0/(45-7)	55.1/(45-7)
χ^2/dof	—	7.6	2.8	1.25	1.26	1.24	1.45

The choice of ϵ_{11}, $\widetilde{\lambda}_f$, as well as the hyperfine splittings $\Delta\varepsilon_{d\mu}^F$ and $\Delta\varepsilon_{dd\mu}^S$, was motivated by the possibility to compare them with direct theoretical calculations of these quantities. The necessity for renormalization of the hyperfine transition rate $\lambda_{21}^{\mathrm{sc}}$ (factor C_{21}) was discussed already in the previous Section. The rescaling of matrix elements $|V_{if}|$ (factor C_m) was introduced to take into account potentially insufficient precision in the matrix elements [66] and in the asymptotic normalization of the $dd\mu$ wave function at large internuclear distances [66,73]. The renormalization of the rotational energies $\varepsilon(K_f) \equiv E_{7K_f}$ of the MD complex should take into account uncertainties in calculating these energies at high vibrational quantum number ($\nu = 7$) in [69], and also a possibility that only partial thermalization of the rotational states is achieved before back decay [74].

The experimental data (45 experimental points presented in Tables 7 and 9) were simultaneously fitted with the calculated $\widetilde{\lambda}_{dd\mu}^F(T)$ (Eq. (28)) and $\widetilde{\lambda}_{21}(T)$ (Eq. (29)) over the whole temperature range from $T = 28$ K to $T = 350$ K. An ortho/para ratio of D$_2$ molecules equal to 2.4 (Eq. (35)) was assumed that corresponds to equilibrium mixture at 77 K. The number of fitting parameters was varied from four (Fit A) to five (Fit B) and seven (Fit C). The numerical results of the fits are presented in Table 13. The $dd\mu$ formation rates $\widetilde{\lambda}_{dd\mu}^F(T)$ obtained in Fits A, B, and C are presented in Fig. 24 in comparison with the experimental data, while Fig. 21 shows spin flip rates obtained in Fit C. The best results were obtained in Fit C. In this case, the calculated formation rates $\widetilde{\lambda}_{dd\mu}^{3/2}(T)$, $\widetilde{\lambda}_{dd\mu}^{1/2}(T)$, as well as the spin flip rate $\widetilde{\lambda}_{21}(T)$, fit very well the experimental data in the whole temperature range with the total $\chi^2/\mathrm{dof} = 1.25$. Only statistical errors are shown in Table 13. To estimate systematics errors, additional fits were performed: Fit D in reduced temperature range (28–150 K), Fit E with ortho/para ratio equal to 2.0/1 (statistical mixture at room temperature), and Fit F with pure ortho D$_2$.

In discussing the results of those fits, first a remarkable agreement of the fitted $dd\mu$ energy $\varepsilon_{11}(\mathrm{fit})$ with the theoretical value $\varepsilon_{11}(\mathrm{theory}) = -1.9646(4)$ eV is evident. Table 13 indicates only small variations of $\varepsilon_{11}(\mathrm{fit})$ from –1.9656 eV (Fit A) to –1.9646 eV (Fit C). Therefore, we conclude that the systematic error in $\varepsilon_{11}(\mathrm{fit})$ is ± 0.5 MeV, and the total error is ± 0.7 MeV. By averaging the results from Fit A, Fit B, and Fit C, we obtain the final result:

$$\varepsilon_{11}(\mathrm{fit}) = -1.9651(7) \text{ eV}.$$

The observed agreement between $\varepsilon_{11}(\mathrm{fit})$ and $\varepsilon_{11}(\mathrm{theory})$ proves the reliability of the theoretical models developed for calculations of both the nonrelativistic energy of the $dd\mu$ ($J = 1$, $v = 1$) state, and also the relativistic and other corrections to this energy shown in Table 12.

The value of the effective fusion rate $\widetilde{\lambda}_f$ found from various fits was quite stable. Again, averaging the results of Fit A–C, we obtain:

$$\widetilde{\lambda}_f(\text{fit}) = 381(15)10^6 \text{ s}^{-1}.$$

This result is $\approx 20\%$ below the theoretical value [37,40,41], which is not beyond the uncertainties of the theoretical calculations.

The striking disagreement of the measured nonresonant spin flip rate with the theoretical predictions ($C_{21} = 0.59(1)$) was already discussed in the previous Section. It requires some revision of the theoretical model [65] used to calculate the nonresonant spin flip rate.

The renormalization of the matrix elements obtained in Fit C ($C_m \approx 0.80$) seems reasonable as the method used to evaluate the widths of quasi-stationary states [66] and to calculate the matrix elements [61] could in general overestimate the magnitude of the matrix elements by 10–20%. But, of course, renormalization of all matrix elements by a single factor is a rough approximation. Further improvements of the scheme for calculating $|V_{if}|$ should be investigated in the future.

In Fit A, there are four free parameters: ε_{11}, $\widetilde{\lambda}_f$, C_m, and C_{21}. Although this fit reproduces the experimental data with maximum deviation of only $\pm 6\%$ (see Fig. 24), its quality is poor with $\chi^2/\text{dof} = 7.5$. Inclusion in the fit of the fifth parameter, C_{MD}, which renormalizes the rotational energy of the $[(dd\mu)dee]^*$ complex with $\nu_f = 7$, greatly improves the quality of the fit with the value of $\chi^2/\text{dof} = 2.8$ (see Fit B in Table 13 and in Fig. 24). Finally, addition of two more free parameters, C_F and C_S, brings the calculated rates $\widetilde{\lambda}_{dd\mu}^{3/2}(T)$, $\widetilde{\lambda}_{dd\mu}^{1/2}(T)$, $\widetilde{\lambda}_{21}(T)$ in good agreement with the experimental data with $\chi^2/\text{dof} = 1.25$ (Fit C in Table 13 and in Figs. 24 and 21). As concerns the scaling factors C_F and C_S of the hyperfine energy splitting in the $d\mu$ atom and in the $dd\mu$ molecule, respectively, they proved to be close to unity, thus supporting the results of theoretical calculations of the HF splitting [38]. The 1.8% deviation of C_F might be within the systematic errors of our analysis. On the other hand, renormalization of the rotational energies of the MD complex appeared essential in this analysis with the value of scaling factor $C_{\text{MD}} \approx 0.8$. While some justification for introducing this scaling factor in the fitting procedure was discussed above, its value seems inconsistent with the stated precision of ~ 0.05 meV of the calculations [69] of ro-vibrational excitations. Thus, taking into account the approximations in our analysis (in particular, in calculations of the matrix elements), we consider this result only as a hint to possible problems in calculations of the ro-vibrational states in the MD complex at high ν values and the thermalization rate of these states.

Concluding this Section, Fig. 25, a compares the previous measurements of the $dd\mu$ formation rates with the best fit to our experimental data. Several ex-
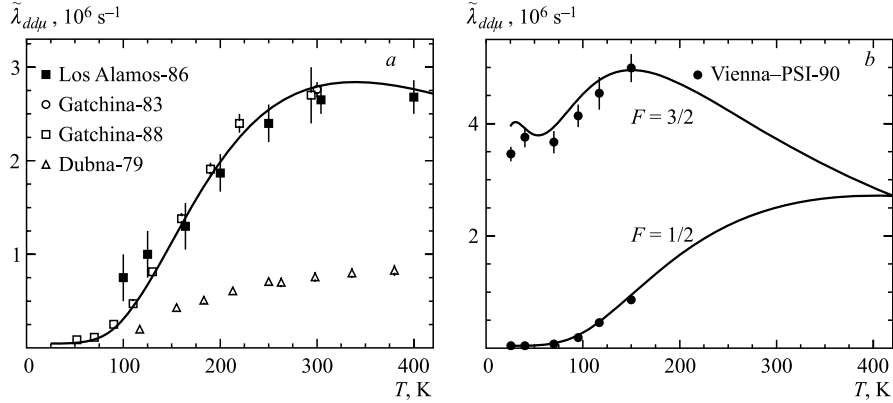
Fig. 25. Comparison of the results of the present experiment (represented by the best fit curves to our experimental data) with the results of previous experiments: *a*) measurements of the steady-state $dd\mu$ formation rate, experiments [18,75,76]; *b*) measurements of hyperfine components of the effective $dd\mu$ formation rate, experiment [16]

periments in Dubna [75], Gatchina [18], and Los Alamos [76] measured only the steady-state $dd\mu$ formation rate. Historically, the Dubna-79 was the first experiment demonstrating the resonant temperature dependence of $\lambda_{dd\mu}$. Unfortunately, the normalization of the neutron detection efficiency was not correct in these measurements. The results of the Gatchina-83, Gatchina-88 and Los Alamos-86 experiments agree with our data within the errors of the previous measurements. Figure 25,*b* presents a similar comparison with the pioneering measurements of the hyperfine formation rates $\lambda_{dd\mu}^{3/2}$ and $\lambda_{dd\mu}^{1/2}$ by the Vienna–PSI collaboration [16]. Taking into account the cited overall normalization error of $\pm 8.5\%$ of these data, the previous measurements are in good agreement with our data. As a cross-check, we have fitted the Vienna–PSI data with our fitting programme (Fit A). The results of the fit, $\varepsilon_{11}(\text{fit}) = -1.9659(2)$ eV and $\widetilde{\lambda}_f(\text{fit}) = 341(36) \cdot 10^6$ s^{-1}, are in reasonable agreement with the values $\varepsilon_{11}(\text{fit}) = -1.9661(2)$ eV and $\widetilde{\lambda}_f(\text{fit}) = 314(33) \cdot 10^6$ s^{-1} quoted in the original work and with the results of our Fit A.

6. SUMMARY

A new experimental method using a time-projection hydrogen ionization chamber was applied for studies of muon catalyzed dd fusion in D₂ and HD gases in the temperature range from 28 to 350 K. In a series of experiments performed in a high intensity muon beam at PSI, the main observables in the

$dd\mu$ fusion were measured with high absolute precision:

— The resonant $dd\mu$ formation rates $\widetilde{\lambda}^{F}_{dd\mu}(T)$.

— The nonresonant $dd\mu$ formation rate $\lambda^{\mathrm{nr}}_{dd\mu}(T)$.

— The spin flip rate in $d\mu$ atoms $\widetilde{\lambda}_{21}(T)$.

— The branching ratio of the two charge symmetric channels $R(T)$.

— The muon sticking probability ω_d.

The obtained set of data presents a basis for a quantitative comparison with the theoretical calculations of various processes involved in $dd\mu$ fusion.

The experimental data on $\widetilde{\lambda}^{F}_{dd\mu}(T)$ and $\widetilde{\lambda}_{21}(T)$ provide a critical test of the theory of resonant formation of the $dd\mu$ molecule which is the key element of the μCF phenomenon. Our experimental data were compared with the results of the theoretical approach [37], where the rates $\widetilde{\lambda}^{F}_{dd\mu}(T)$ and $\widetilde{\lambda}_{21}(T)$ have been calculated without any free parameter, all the physical inputs needed being taken exclusively from theoretical considerations. This *ab initio* theory is in *qualitative* agreement with the experimental data, as can be seen in Fig. 24. On the other hand, the high precision and large number of experimental points over a wide temperature range in our experiment allowed one to extract some of the input parameters directly from the fit to the experimental data and to *quantitatively* compare them with the theoretical predictions. Table 13 presents seven input parameters determined in this way. Some of them proved to be in close agreement with the theoretical values. These are: the energy ε_{11} of the $dd\mu$ molecule, the hyperfine splitting in the $d\mu$ atom and in the $dd\mu$ molecule, and the fusion rate $\widetilde{\lambda}_f$ from the ($J = 1$, $v = 1$) state of the $dd\mu$ molecule. On the contrary, the matrix elements of transitions from the $d\mu$+D_2 system to the $[(dd\mu)dee]^*$ complex were found by a factor of 0.8 below the theoretical values. Also, the rotational energies of the $[(dd\mu)dee]^*$ complex in the ($\nu = 7$, K_f) states proved to be below the theoretical values by a factor of 0.73. These results indicate the directions where the theory of muon catalyzed dd fusion, being in general very successful in describing this phenomenon, could be further developed. A serious problem in the theory of the spin flip in nonresonant collisions of $d\mu$ atoms with D_2 molecules was found, in agreement with experiment [16]. The theoretical spin flip rates appear to be by a factor of 1.7 higher than the measured ones. Up to now, this theoretical problem remains unexplained.

The most important parameter extracted from the fits is the energy of the least bound state ($J = 1$, $v = 1$) of the $dd\mu$ molecule, $\varepsilon_{11}(\mathrm{fit}) = -1.9651(7)$ eV, which proved to be in impressive agreement with the theoretical value $\varepsilon_{11}(\mathrm{theory}) = -1.9646(4)$ eV. This agreement demonstrates the validity of the theoretical calculations of both the nonrelativistic part of ε_{11} and also the relativistic and other corrections to this value shown in Table 12.

Our HD experiment provided information on the nonresonant $dd\mu$ formation rate $\lambda^{\mathrm{nr}}_{dd\mu}(T)$. It was shown that this rate increases slowly with temperature,

remaining still rather small ($< 0.1 \cdot 10^6$ s^{-1}) in the measured temperature range $50 < T < 300$ K. However, at epithermal energies of the $d\mu$ atoms ($E_{d\mu} > 1$ eV), this rate becomes an order of magnitude higher, as demonstrated by prominent sharp peaks in the initial part of time distributions of the dd fusion neutrons (Fig. 18). The simultaneous measurement of the branching ratio $R = Y(^3\text{He} + n)/Y(t+p)$ allowed one to decompose $\lambda_{dd\mu}^{\text{nr}}(T)$ in two components, $\lambda_{J=1}^{\text{nr}}(T)$ and $\lambda_{J=0}^{\text{nr}}(T)$, corresponding to formation of the $dd\mu$ molecule in the $J = 1$ and $J = 0$ states, respectively. The ratio of these components was found to be constant in the measured temperature range. The theory of nonresonant $dd\mu$ formation is in general agreement with our experimental data, with the exception of the $E0$ transitions from the $d\mu + \text{HD}$ system to the $dd\mu$ molecule, where the measured rates appeared to be a factor of 2 higher than predicted.

A strong asymmetry was observed in the ratio of the yields of the charge symmetric fusion channels following resonant $dd\mu$ formation ($R = 1.445$), while the nonresonant $dd\mu$ formation leads to dd fusion with $R = 1.0$. This surprising nuclear phenomenon was explained by Hale [59] in a theory assuming a special mechanism of enhancement of the Coulomb isospin mixing in the P states of the ^{4}He nucleus.

Our measurements of the muon sticking probability $\omega_d(\text{exp.}) = 0.1224(6)$ for gas density $\varphi = 0.0837$, control with high precision both the theory of initial muon sticking and also the theory of the muon reactivation during slowing down of the $^3\text{He}\mu$ atom. It was demonstrated that the theory describes adequately the experimental data. The close agreement of the theoretical calculations of $\omega_d(\text{theory}) = 0.123(4)$ with experiment supports the expectation that similar calculations of the muon sticking probability in $dt\mu$ fusion should be correct as well: $\omega_t(\text{theory}) = (0.7 \to 0.6)\%$ for gas density $\varphi = (0.05 \to 1.2)$ [77]. The available experimental data are in agreement with this prediction, with the most precise result $\omega_t(\text{exp.}) = (0.58 \pm 0.04)\%$ at $\varphi = 0.17$ [19]. The obtained values for ω_t define an upper limit of ≈ 200 for the mean number of $dt\mu$ fusion cycles that could be catalyzed by one muon.

REFERENCES

1. *Breunlich W. H. et al.* // Ann. Rev. Nucl. Part. Sci. 1989. V. 39. P. 311;
   Gershtein S. S., Petrov Yu. V., Ponomarev L. I. // Usp. Fiz. Nauk. 1990. V. 160. P. 3;
   Ponomarev L. I. // Contemp. Phys. 1990. V. 31. P. 219;

Men'shikov L. I. // Usp. Fiz. Nauk. 1990. V. 160. P. 47;
Froelich P. // Adv. Phys. 1992. V. 41. P. 405;
Petitjean C. // Nucl. Phys. A. 1992. V. 543. P. 79;
Ponomarev L. I. // Hyp. Int. 2001. V. 138. P. 15.

2. *Frank F. C.* // Nature. 1947. V. 160. P. 525.
3. *Lattes C. M. G., Occhialini G. P. S., Powell C. F.* // Ibid. P. 453.
4. *Sakharov A. D.* // Rep. Phys. Inst. Acad. Sci. USSR. 1948;
   Sakharov A. D. // Muon Cat. Fus. 1989. V. 4. P. 235 and Comments by *Gershtein S. S., Ponomarev L. I.* // Ibid. P. 241.
5. *Zeldovich Ya. B.* // Dokl. AN SSSR. 1954. V. 95. P. 493.
6. *Alvarez L. W. et al.* // Phys. Rev. 1957. V. 105. P. 1127.
7. *Fetkovich J. G. et al.* // Phys. Rev. Lett. 1960. V. 4. P. 570.
8. *Doede J.* // Phys. Rev. 1963. V. 132. P. 1782.
9. *Zeldovich Ya. B., Gershtein S. S.* // Usp. Fiz. Nauk. 1960. V. 71. P. 581.
10. *Dzhelepov V. P. et al.* // Zh. Eksp. Teor. Fiz. 1966. V. 50. P. 1235.
11. *Vesman E. A.* // Pis'ma ZhETF. 1967. V. 5. P. 113; JETP Lett. 1967. V. 5. P. 91.
12. *Ponomarev L. I., Puzynin I. V., Puzynina T. P.* // J. Comp. Phys. 1973. V. 13. P. 1;
    Vinitsky S. I. et al. JINR Commun. P4-10336. Dubna, 1976.
13. *Vinitsky S. I. et al.* // Zh. Eksp. Teor. Fiz. 1978. V. 74. P. 849.
14. *Bystritski V. M. et al.* // Pis'ma ZhETF. 1979. V. 31. P. 249; Phys. Lett. B. 1980. V. 94. P. 476; Zh. Eksp. Teor. Fiz. 1981. V. 80. P. 1700.
15. *Gershtein S. S., Ponomarev L. I.* // Phys. Lett. B. 1977. V. 72. P. 80.
16. *Kammel P. et al.* // Phys. Lett. B. 1982. V. 112. P. 319; Phys. Rev. A. 1983. V. 28. P. 2611;
    Zmeskal J. et al. // Phys. Rev. A. 1990. V. 42. P. 1165.
17. *Scrinzi A. et al.* // Phys. Rev. A. 1993. V. 47. P. 4691.
18. *Balin D. V. et al.* // Phys. Lett. B. 1983. V. 141. P. 173;
    Balin D. V. et al. // Pis'ma ZhETF. 1984. V. 40. P. 318;
    Balin D. V. et al. // Pis'ma ZhETF. 1985. V. 42. P. 236;
    Vorobyov A. A. // Muon Cat. Fus. 1988. V. 2. P. 17;
    Balin D. V. et al. // Muon Cat. Fus. 1990/1991. V. 5/6. P. 163.
19. *Case T. A. et al.* // Hyp. Int. 1999. V. 118. P. 197.
20. *Ackerbauer P. et al.* // Phys. Lett. B. 1998. V. 417. P. 224.
21. *Voropaev N. I. et al.* // Hyp. Int. 2001. V. 138. P. 331; PNPI Preprint PNPI-2444. 2001. P. 1–55;
    Balin D. V. et al. PNPI Preprint PNPI-2729. 2007. P. 1–88.
    Voropaev N. I. et al. // Proc. of the Intern. Conf. on Muon Cat. Fusion and Related Topics. Dubna, 2007. P. 67–81.
22. *Markushin V. E.* // Hyp. Int. 1999. V. 119. P. 11.
23. *Faifman M. P., Men'shikov L. I.* // Hyp. Int. 2001. V. 138. P. 61.
24. *Schottmüller J. et al.* // Hyp. Int. 1999. V. 119. P. 95.
25. *Lauss B. et al.* // Phys. Rev. Lett. 1998. V. 80. P. 3041; Phys. Rev. A. 1999. V. 60. P. 209.
26. *Pohl R. et al.* // Hyp. Int. 2001. V. 138. P. 35.

27. *Men'shikov L. I., Ponomarev L. I.* // Pis'ma ZhETF. 1985. V. 42. P. 12; JETP Lett. 1985. V. 39. P. 13.
28. *Lauss B. et al.* // Phys. Rev. Lett. 1996. V. 76. P. 4693.
29. *Lauss B. et al.* // Hyp. Int. 1999. V. 118. P. 79.
30. *Bleser E. I. et al.* // Phys. Rev. 1963. V. 132. P. 2679;
    Dzhelepov V. P. et al. // Zh. Eksp. Teor. Fiz. 1966. V. 50. P. 1235; JETP. 1966. V. 23. P. 820;
    Cohen J. S., Struensee M. C. // Phys. Rev. A. 1991. V. 43. P. 3460;
    Cohen J. S. // Hyp. Int. 1993. V. 82. P. 15;
    Kobayashi K., Ishihara T., Toshima N. // Muon Cat. Fus. 1988. V. 2. P. 191.
31. *Adamczak A.* // Hyp. Int. 1996. V. 101/102. P. 113.
32. *Adamczak A., Faifman M. P.* // Eur. Phys. J. D. 2009. V. 51. P. 341.
33. *Vinitsky S. I., Puzynin I. V.* // Muon Cat. Fus. 1988. V. 3. P. 307.
34. *Korobov V. I.* // J. Phys. B. 2004. V. 37. P. 2331.
35. *Lane A. M.* // Phys. Lett. A. 1983. V. 98. P. 337.
36. *Leon M.* // Phys. Rev. A. 1986. V. 33. P. 4434.
37. *Men'shikov L. I. et al.* // Zh. Eksp. Teor. Fiz. 1987. V. 92. P. 1173.
38. *Bakalov D.* // Muon Cat. Fus. 1988. V. 3. P. 321.
39. *Gershtein S. S.* // Zh. Eksp. Teor. Fiz. 1958. V. 34. P. 463; Sov. Phys. JETP. 1958. V. 7. P. 318; Zh. Eksp. Teor. Fiz. 1961. V. 40. P. 698; Sov. Phys. JETP 1961. V. 13. P. 488.
40. *Bogdanova L. et al.* // Phys. Lett. B. 1982. V. 115. P. 171; 1986. V. 167. P. 485.
41. *Bakalov D. et al.* // Zh. Eksp. Teor. Fiz. 1988. V. 94. P. 61.
42. *Thalmann Y. A. et al.* // Phys. Rev. A. 1998. V. 57. P. 1713.
43. *Suzuki T., Measday D. F., Roalsvig J. P.* // Phys. Rev. C. 1987. V. 35. P. 2212.
44. *Imao H. et al.* // Phys. Lett. B. 2008. V. 658. P. 120.
45. *Petitjean C. et al.* // Muon Cat. Fus. 1990/1991. V. 5/6. P. 199.
46. *Jackson J. D.* // Phys. Rev. 1957. V. 106. P. 330.
47. *Gershtein S. S. et al.* // Zh. Eksp. Teor. Fiz. 1981. V. 80. P. 1690.
48. *Bogdanova L. N. et al.* // Phys. Lett. B. 1985. V. 161. P. 1.
49. *Hu C. Y., Kauffmann S. K.* // Phys. Rev. A. 1987. V. 36. P. 5420.
50. *Haywood S. E., Monkhorst H. J., Alexander S. A.* // Phys. Rev. A. 1991. V. 43. P. 5847.
51. *Struensee M. C., Cohen J. S.* // Phys. Rev. A. 1988. V. 38. P. 44;
    Cohen J. // Muon Cat. Fus. 1988. V. 3. P. 421.
52. *Markushin V. E.* // Ibid. P. 395.
53. *Takahashi H.* // Ibid. P. 453.
54. *Abramov D. I. et al.* // Hyp. Int. 1996. V. 101/102. P. 301.
55. *Frolov A. M.* // Phys. Lett. A. 2001. V. 291. P. 274.
56. *Men'shikov L. I., Ponomarev L. I.* // Pis'ma ZhETF. 1985. V. 41. P. 511; JETP Lett. 1985. V. 41. P. 623.
57. *Adyasevich B. P. et al.* // Yad. Fiz. 1981. V. 33. P. 1167.
58. *Bogdanova L. N.* // Muon Cat. Fus. 1988. V. 3. P. 359.
59. *Hale G. M.* // Muon Cat. Fus. 1990/1991. V. 5/6. P. 227.

60. *Faifman M. P.* // Muon Cat. Fus. 1989. V. 4. P. 341.
61. *Faifman M. P. et al.* // Hyp. Int. 1996. V. 101/102. P. 179.
62. *Aschenauer E. C., Markushin V. E.* // Ibid. P. 97.
63. *Markushin V. E. et al.* PSI Preprint PSI-PR-92-26.
64. *Melezhik V. S., Wozniak J.* JINR Commun. E4-96-113. Dubna, 1996.
65. *Adamczak A. et al.* // At. Data and Nucl. Data Tables. 1996. V. 62. P. 255.
66. *Men'shikov L. I., Faifman M. P.* // Yad. Fiz. 1985. V. 43. P. 650; Sov. Phys. Nucl. Phys. 1986. V. 43. P. 414;
    Faifman M. P., Men'shikov L. I., Strizh T. A. // Muon Cat. Fus. 1989. V. 4. P. 1.
67. *Petrov Yu. V.* // Nature. 1980. V. 285. P. 466;
    Petrov Yu. V., Petrov V. Yu. // Zh. Eksp. Teor. Fiz. 1991. V. 100. P. 56; Sov. Phys. JETP. 1991. V. 73. P. 29;
    Petrov Yu. V. et al. // Phys. Rev. A. 1998. V. 57. P. 1636;
    Petrov Yu. V., Petrov V. Yu. nucl-th/0108068v1. 2001.
68. *Faifman M. P. et al.* // Z. Phys. D. 1986. V. 2. P. 79.
69. *Scrinzi A., Szalewicz K., Monkhorst H. J.* // Phys. Rev. A. 1988. V. 37. P. 2270.
70. *Bakalov D., Korobov V. I.* // Hyp. Int. 2001. V. 138. P. 265.
71. *Harston M. R. et al.* // Phys. Rev. A. 1997. V. 56. P. 2685.
72. *Melezhik V. S., Ponomarev L. I.* // Phys. Lett. B. 1978. V. 77. P. 217.
73. *Kino Y. et al.* // Phys. Rev. A. 1995. V. 52. P. 870.
74. *Padial N. T., Cohen J. S., Walker R. B.* // Phys. Rev. A. 1988. V. 37. P. 329;
    Padial N. T., Cohen J. S., Leon M. // Ibid. V. 38. P. 1172.
75. *Bystritskii V. M. et al.* // Zh. Eksp. Teor. Fiz. 1979. V. 76. P. 460; Sov. Phys. JETP. 1979. V. 49. P. 232.
76. *Jones S. E. et al.* // Phys. Rev. Lett. 1986. V. 56. P. 588.
77. *Kamimura M., Hiyama E., Kino Y.* // Hyp. Int. 1999. V. 118. P. 217;
    Stodden C. D. et al. // Phys. Rev. A. 1990. V. 41. P. 1281.